Monthly Notices of the ROYAL ASTRONOMICAL SOCIETY

MNRAS **527,** 6253–6275 (2024) https://doi.org/10.1093/mnras/stad2953
Advance Access publication 2023 September 27

Survey of gravitationally lensed objects in HSC imaging (SuGOHI) – IX. Discovery of strongly lensed quasar candidates

James H. H. Chan [1,2★] Kenneth C. Wong [3] Xuheng Ding [4] Dani Chao,[5] I-Non Chiu [6] Anton T. Jaelani [7,8] Issha Kayo [9] Anupreeta More [4,10] Masamune Oguri[11,12] and Sherry H. Suyu[13,14,15]

[1]*Department of Astrophysics, American Museum of Natural History, Central Park West and 79th Street, NY 10024-5192, USA*
[2]*Department of Physics and Astronomy, Lehman College of the CUNY, Bronx, NY 10468, USA*
[3]*National Astronomical Observatory of Japan, 2-21-1 Osawa, Mitaka, Tokyo 181-8588, Japan*
[4]*Kavli Institute for the Physics and Mathematics of the Universe (Kavli IPMU, WPI), The University of Tokyo, Chiba 277-8583, Japan*
[5]*Ruđer Bošković Institute, Bijenička Cesta 54, 10000 Zagreb, Croatia*
[6]*Department of Astrophysics, National Cheng Kung University, No.1, University Road, Tainan City 701, Taiwan*
[7]*Astronomy Research Group and Bosscha Observatory, FMIPA, Institut Teknologi Bandung, Jl. Ganesha 10, Bandung 40132, Indonesia*
[8]*U-CoE AI-VLB, Institut Teknologi Bandung, Jl. Ganesha 10, Bandung 40132, Indonesia*
[9]*Department of Liberal Arts, Tokyo University of Technology, Ota-ku, Tokyo 144-8650, Japan*
[10]*The Inter-University Center for Astronomy and Astrophysics, Post bag 4, Ganeshkhind, Pune 411007, India*
[11]*Center for Frontier Science, Chiba University, 1-33 Yayoi-cho, Inage-ku, Chiba 263-8522, Japan*
[12]*Department of Physics, Graduate School of Science, Chiba University, 1-33 Yayoi-Cho, Inage-Ku, Chiba 263-8522, Japan*
[13]*Technical University of Munich, TUM School of Natural Sciences, Department of Physics, James-Franck-Straße 1, D-85748 Garching, Germany*
[14]*Max-Planck-Institut für Astrophysik, Karl-Schwarzschild-Str. 1, D-85748 Garching, Germany*
[15]*Academia Sinica Institute of Astronomy and Astrophysics (ASIAA), 11F of ASMAB, No.1, Section 4, Roosevelt Road, Taipei 10617, Taiwan*

Accepted 2023 September 22. Received 2023 September 22; in original form 2023 April 14

ABSTRACT

We report the discovery of new lensed quasar candidates in the imaging data of the Hyper Suprime-Cam Subaru Strategic Program (HSC-SSP) Data Release 4, covering 1 310 deg^2 of the sky with median seeing in the *i* band of ≈0.6 arcsec. In addition to two catalogues of Million Quasars Catalog v7.2 and AllWISE Catalog of Mid-Infra Red Active Galactic Nuclei, containing confirmed and candidate quasars, we preselect quasar sources using colour cuts from the HSC (*grizy*) and unWISE ($W1 + W2$) photometric data based on SDSS spectroscopic catalogues. We search for the presence of multiple point sources with similar colour through the convolution of the Laplacian of the preselected quasar image cutouts with the Laplacian of the point spread function, resulting in a reduction of lens candidates from 1 652 329 to 121 511 (7.4 per cent). After visual binary classification, we grade 6 199 (0.4 per cent) potential lenses on a scale of 0 to 3, with 3 indicating a lens and 0 indicating a non-lens. Finally we obtain 162 lens candidates with an average grade of ≥2, and among them, we successfully recover 18 known lenses. By fitting the light distribution and removing the known contaminants, we discover that 57 new systems contain at least two point sources and a galaxy in between, including 10 possible quadruply lensed quasars. This new sample exhibits a median separation of 1.26 arcsec and a magnitude limit of $i \approx 22$. Spectroscopic or high-resolution imaging follow up on these newly discovered lensed quasar candidates will further allow their natures to be confirmed.

Key words: gravitational lensing: strong – (galaxies:) quasars: general.

1 INTRODUCTION

Gravitationally lensed quasars are valuable astronomical objects that offer unique opportunities for studying galaxy evolution and cosmology. This phenomenon occurs when a foreground galaxy bends the light coming from a distant quasar, through the gravitational lensing effect. In the case of strong lensing, this can produce highly distorted, magnified, and even multiple images of the same quasar source and its host galaxy. The image configurations of these systems provide insights into the mass structures and sub-structures of the lensing galaxies, which can further inform our understanding of galaxy evolution in the Universe (e.g. Dalal & Kochanek 2002; Suyu et al. 2012; Vegetti et al. 2012; Nierenberg et al. 2017; Gilman et al. 2019). Additionally, the time delays between the lensed images can be used to infer the Hubble constant, H_0, a crucial cosmological parameter that determines the size, age, and critical density of the Universe (e.g. Refsdal 1964; Chen et al. 2019; Wong et al. 2020). Given the current discrepancy between H_0 measurements from the early and late Universe, independent measurements from lensed quasars are of vital importance (e.g. Verde, Treu & Riess 2019; Freedman 2021;Di Valentino et al. 2021). Therefore,

★ E-mail: jchan@amnh.org

lensed quasars provide a powerful tool for understanding the Universe's fundamental properties, making them a subject of significant interest.

To date, approximately 300 gravitationally lensed quasars have been identified. The largest statistical sample of radio-loud lensed quasars was provided by the Cosmic Lens All-Sky Survey (Myers et al. 2003), which identified flat-spectrum radio sources with multiple lensed images. From optical data, the SDSS Quasar Lens Search (SQLS; Oguri et al. 2006, 2008, 2012; Inada et al. 2008, 2010, 2012) discovered 62 lenses using morphological and colour selection of spectroscopically confirmed quasars. Jackson et al. (2012) extended the SQLS sample by utilizing better image quality from the UKIRT Infrared Deep Sky Survey (Lawrence et al. 2007).

With the increasing depth and quality of ongoing surveys, it is now possible to identify lensed quasars from imaging alone without spectroscopic preselection. For instance, data mining on catalogued magnitudes to identify multiple quasar sources enables the discovery of lensed quasars in various surveys, such as the Dark Energy Survey (Agnello et al. 2018), the Kilo Degree Survey (Spiniello et al. 2018; Khramtsov et al. 2019), and the DESI Legacy Imaging Surveys (Dawes et al. 2022; He et al. 2023). To avoid contaminants, Lemon et al. (2018) and Lemon, Auger & McMahon (2019) used simultaneous optical-infrared extracted colours in combination with astrometric measurements from *Gaia*. This method has confirmed 86 new lensed quasars (Lemon et al. 2022), which expand the previous sample size by a factor of 1.5. Additionally, thanks to the exceptional spatial resolution of *Gaia*, the catalogued image positions have been used to identify new lenses (Krone-Martins et al. 2018; Ducourant et al. 2018a, b).

Chan et al. (2015) demonstrated an image-based search approach using CHITAH – an automated pixel- and mass-modelling code for finding lensed quasars. Other image-based lens finding strategies have relied on machine learning, ring-finders, and citizen science. These lens searches aim to find lenses, including lenses at both galaxy- and cluster-mass scales, in the Survey of Gravitationally lensed Objects in Hyper Suprime-Cam (HSC) Imaging (SuGOHI; Sonnenfeld et al. 2018, 2019, 2020; Wong et al. 2018, 2022; Chan et al. 2020; Jaelani et al. 2020, 2021). However, this has mainly had success for lensed galaxies where the extended lensed arcs are distinguishable from other astrophysical objects. In the case of lensed quasars, often just two point sources are present which outshine the light from the lensing galaxy, and are outnumbered by visually similar contaminants like binary stars, or quasar-star projections.

Here, we continue a search for lensed quasars in the HSC Data Release 4 (DR4) imaging data, using the Laplacian of an image for better point source detection. This method has been applied in the Canada–France Imaging Survey (CFIS; Ibata et al. 2017) Data Release 2 data and successfully discovered five doubly imaged lensed quasars (Chan et al. 2022). We expect that still many lenses are yet to be discovered in the HSC survey, either due to poor point source detection or strict preselection criteria of previous search methods that discarded lensed quasars from the sample. The resulting sample of lensed quasars presented in this work is considered a subset of the 'SuGOHI-q' lens sample.

This paper is organized as follows: We provide descriptions of the HSC data and the quasar selection in Section 2. The automated part of our lens search method is described in Section 3, while the visual inspection is discussed in Section 4. We outline the light and lens modellings for the high-grade candidates in Section 5. We present the result and discuss the individual systems in Section 6. We conclude our findings in Section 7. All images are oriented with North up and East left. Optical magnitudes quoted in this paper are in the AB system, and infrared magnitudes (specifically *W*1 and *W*2 from the *WISE* survey) in the Vega system.

2 DATA

We preselect quasar sources and look into their images in order to identify lens candidates. In this section, we first describe the HSC imaging data (Section 2.1), and then the selection methods for potential quasar sources (Section 2.2).

2.1 HSC imaging

The HSC Subaru Strategic Program (HSC-SSP; Aihara et al. 2018) is a three-layered and multi-band imaging survey with the HSC (Miyazaki et al. 2018) on the 8.2m Subaru Telescope. The wide layer of the HSC-SSP consists of five broad-band filters (*grizy*) with a depth of $z \approx 26$ (5σ for point sources) and a pixel scale of 0.168 arcsec. In this work, we take the data set from DR4, which comprises data obtained up to the semester S21A and covers 1 310 deg^2 in full colour, including 984 deg^2 to the full depth. The footprint of HSC DR4 S21A is illustrated in Fig. 1. The median seeing in the *i* band is about 0.6 arcsec. The data have been processed with the pipeline `hscPipe8.4` (Bosch et al. 2018). In this work, we generate cutouts of science and variance images with a size of 7.56 arcsec × 7.56 arcsec (45 pixels on a side), and cutouts of point spread function (PSF) with size of 5.21 arcsec × 5.21 arcsec (31 pixels on a side).

2.2 Catalogues

The standard way of selecting large numbers of quasar candidates is to determine 'colour cuts' via optical (or infrared) photometry (e.g. Wu et al. 2012; Peters et al. 2015). In order to determine the cuts, we use the spectroscopic classification in SDSS DR16 (Ahumada et al. 2020), containing stars, galaxies, and quasars. We then perform a cross-match search, within radii of 1 arcsec and 2 arcsec to acquire HSC (*grizy*) photometry and unWISE (*W*1/2) photometry (Schlafly, Meisner & Green 2019), respectively. A larger tolerance is applied for the infrared photometry to account for the larger angular resolution (>5 arcsec) in the *WISE* survey (Wright et al. 2010). We only select the objects with a magnitude of $i < 22$, and the colour–colour diagrams are shown in Fig. 2. For the quasar selection, we apply the colour cuts of

$$g - r < 1, \quad r - i < 1, \quad i - z < 0.75, \quad z - y > -0.5,$$
$$y - W1 > 2, \quad y - W2 > 3, \text{ and } \quad W1 - W2 > 0, \tag{1}$$

which enable us to remove ≈ 97 per cent stars and to preserve ≈ 95 per cent quasars. The numbers of the SDSS sample are listed in Table 1. We notice that the majority of selected quasars exhibit redshifts $z < 3.5$ as shown in Fig. 3, which is in agreement with the finding in Wu et al. (2012). The same colour and magnitude cuts are applied in the HSC DR4 S21A for our quasar sample preselection. For the reliable HSC PSF photometry, we include the conditions in the query:

```
isprimary
AND NOT (grizy)_pixelflags_interpolatedcenter
AND NOT (grizy)_pixelflags_saturatedcenter
AND NOT (grizy)_pixelflags_crcenter
AND NOT (grizy)_pixelflags_bad.
```
(2)

After cross matching the unWISE catalogue, we end up with 1587 892 objects.

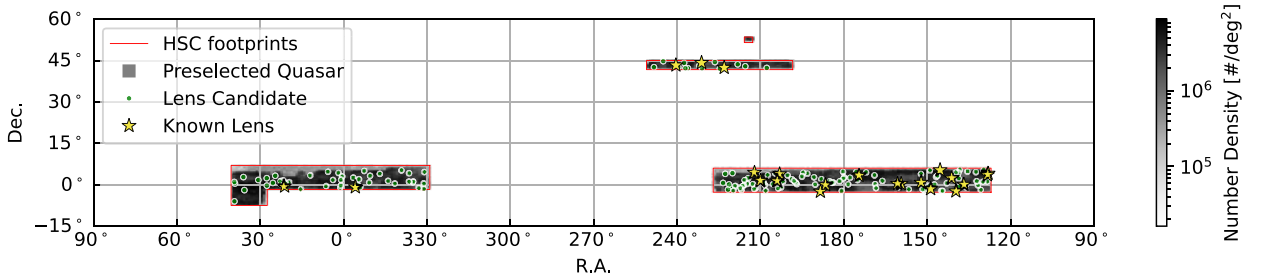

Figure 1. Population on the HSC DR4 S21A footprints. The colourbar represents the number density of preseleted quasar sources. The lens candidates ($G_{\rm av} \geq 2$) found in this work and the known lensed quasars are labelled as green dots and yellow stars, respectively.

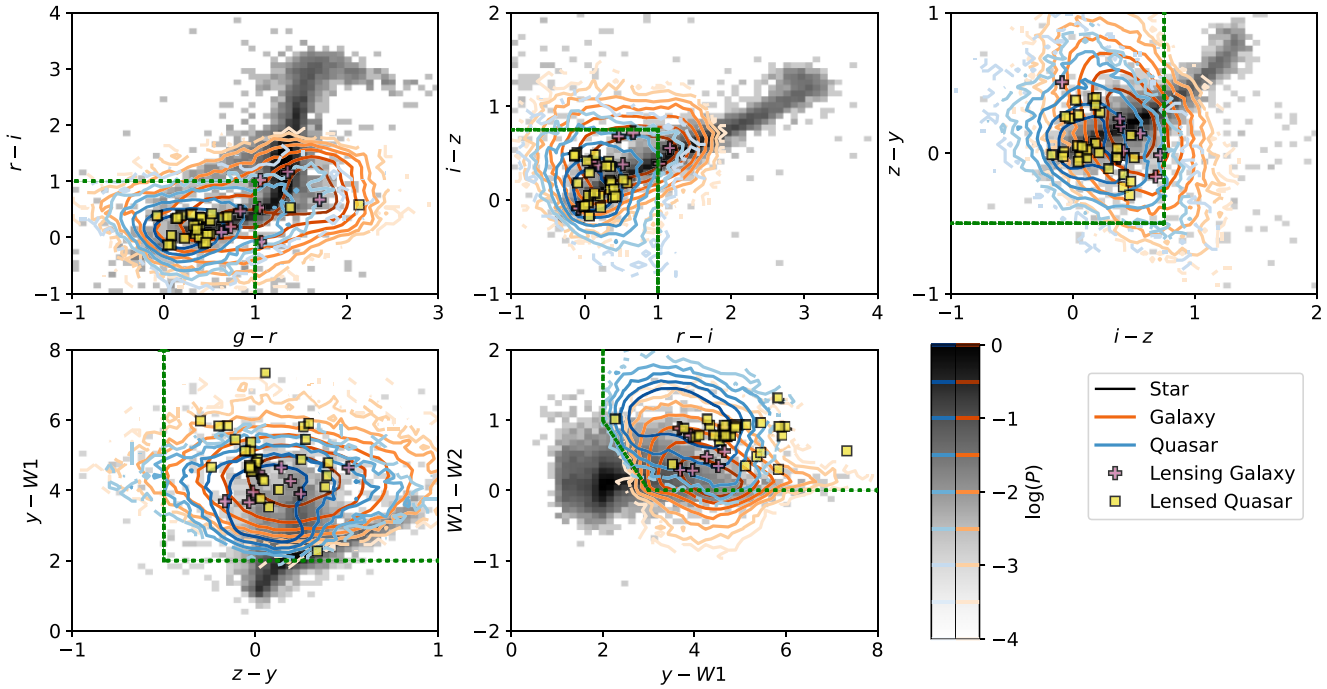

Figure 2. Colour–colour diagrams of the SDSS spectroscopic samples using the HSC and unWISE photometries. The colour cuts applied in this work for the separation of quasars and stars are highlighted with green dotted lines, which exclude 97 per cent of stars and preserve 95 per cent of quasars. The colourbars represent the scaled number density (P) with a maximum value of 1. The known lens systems are decomposed into two components (if available in the HSC catalogue): lensing galaxies and lensed quasar images, as shown in Fig. 5. Two lensed quasar images are failed within the colour cuts due to high redshift (BRI0952−0115) and contamination by the lensing galaxy (one of the images in B1600+434).

Table 1. SDSS spectroscopic sample and known lenses. The total number of objects before and after applying the colour cuts is displayed. The colour cuts are detailed in Section 2.2 and illustrated in Fig. 2, in order to effectively separate quasars and stars. The sample of known lenses is decomposed into two components (if available): lensing galaxies and lensed quasar images.

Type	$i < 22$	Colour-cut	(per cent)
Star	13 164	383	2.91
Galaxy	254 464	65 487	25.74
Quasar	60 827	58 060	95.45
Lensing galaxy	8	3	37.50
Lensed quasar	28	26	92.86

In addition, we include two existing quasar catalogues to slightly expand our sample size. The first one is the Million Quasars Catalog v7.2 (hereafter MILLIQUAS; Flesch 2021), which provides a compilation of both confirmed and candidate quasars from the literature to 2021 December 31. The other catalogue is the complete AllWISE Catalog of Mid-Infra Red Active Galactic Nuclei (hereafter AllWISEAGN; Secrest et al. 2015), which provides the sources with their apparent magnitude distribution peak at $g \approx 20$, extending to objects as faint as $g \approx 26$.

In Table 2, we list the number of objects in each catalogue. To eliminate duplicates and assess the overall performance, we perform a cross-match of the three catalogues within a 2 arcsec radius, and the total number is displayed in the last row.

3 METHOD

Our classification algorithm for detecting lensed quasars relies on identifying systems with multiple point sources of similar colour, which is a common characteristic in a lensed quasar. This method has been successfully applied to the CFIS, resulting in the discovery of several new lenses (Chan et al. 2022). We adopt a modified version

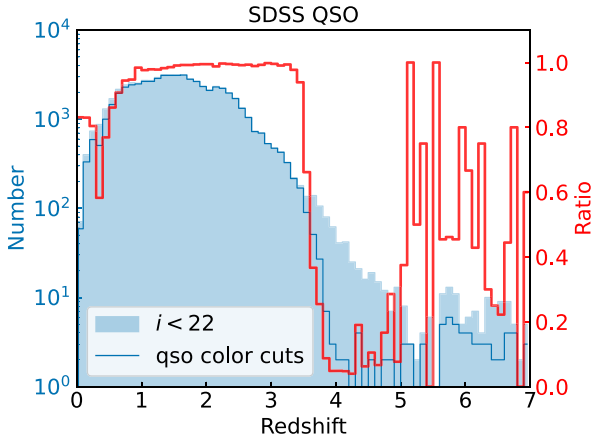

Figure 3. Ratio of SDSS quasars against redshifts via the colour cuts. The sharp drop at redshift ≈3.5 suggests restriction on quasar sample using the colour-cut selection in this work.

of the procedure to better suit the HSC imaging. The following is a brief description of our modified procedure:

(i) *Model HSC PSF with an elliptical Moffat:* The PSFs from the HSC data base can be slightly off-centred or perturbed by higher moments, which can make it difficult to accurately identify point sources [Step (iii)] or measure their fluxes [Step (vi)]. To address this issue, we characterize the HSC data base PSFs using an elliptical Moffat profile (Moffat 1969):

$$I(x, y) = \frac{\beta - 1}{\pi \sigma_x \sigma_y \left(1 + \xi^2\right)^{\beta}}, \tag{3}$$

where σ_x, σ_y, and β are seeing parameters, and ξ is the scale radius with respect to the centre of (x_o, y_o) and the orientation θ:

$$\xi^2 = \left[\frac{(x - x_o)\cos\theta + (y - y_o)\sin\theta}{\sigma_x}\right]^2 + \left[\frac{(x - x_o)\sin\theta - (y - y_o)\cos\theta}{\sigma_y}\right]^2. \tag{4}$$

(ii) *Enhance image and PSF:* The sharpened image $\mathcal{D}_{\rm shp}$ is obtained by convolving the Laplacian of the original image $\mathcal{D}$ with the Laplacian of its corresponding PSF. This convolution enhances point sources in the image, expressed as:

$$\begin{aligned} \mathcal{D}_{\rm shp} &= \Delta\mathcal{D} * \Delta{\rm PSF}, \\ {\rm PSF}_{\rm shp} &= \Delta{\rm PSF} * \Delta{\rm PSF}, \end{aligned} \tag{5}$$

where Δ denotes the Laplacian operator and $*$ is the convolution operator. The sharpening process reduces the Full-Width at Half-Maximum of the PSF by approximately 25 per cent, which enables the more efficient detection of point sources with small separations (see fig. 1 in Chan et al. 2022 and fig. 7 in Cantale et al. 2016 for further details).

(iii) *Identify point sources:* To locate the possible point sources, we use the `DAOStarFinder` python module (Stetson 1987).[1] In addition, a 2D Gaussian fit is required in this process for the local PSF, which corresponds to $\rm PSF_{shp}$ in equation (5). Notably, the Gaussian fit can effectively capture the characteristics of the sharpened Moffat distribution. The output of this process is the positions of identified point sources.

(iv) *Group point sources:* Identifying point sources can vary in different bands. To address this, we collect detections across all bands and group them within their distances less than 1.5 pixels (0.25 arcsec). The final position is then obtained as the mean position of each group.

(v) *Remove systems with one or no identified point sources:* Since a single point source is unlikely to correspond to a lensed quasar system, we exclude any system with one or no point sources detected in the preceding step.

(vi) *Estimate fluxes of point sources:* To determine the colours of each component, we use Powell's minimization method to estimate the flux in each band. This involves placing PSFs at the positions of each component, which is obtained from Step (iii). The PSF is obtained using a Moffat fit, as described in Step (i). The relevant χ^2 value is calculated as follows:

$$\chi^2_{\rm flux} = \frac{1}{N_{\rm band} \cdot N_{\rm pix}} \sum_{grizy} \sum_{i,j} \frac{\left[\mathcal{D}(i, j) - \sum_{k=1}^{n} P_k(i, j)\right]^2}{\mathcal{V}(i, j)}, \tag{6}$$

where $i = 1...N_x$ and $j = 1...N_y$ are the pixel indices of the image cutout with dimensions of $N_x = N_y = 45$, resulting in the total number of pixels $N_{\rm pix} = N_x \cdot N_y$, $N_{\rm band} = 5$ is the total number of bands, $P_k(i, j)$ is the k-th scaled Moffat PSF at the measured position, and $\mathcal{V}(i, j)$ is the pixel variance of $\mathcal{D}(i, j)$ from the HSC data base. We note that the fluxes of lensing galaxies, if they are detected, are likely biased, however this in part cancels out when deriving the colour of the extended component.

(vii) *Remove faint point sources:* To avoid false detections on noise peaks, we exclude point sources that are fainter than the 5σ limiting magnitudes in all bands. The depths of 5σ limiting magnitudes in *grizy* bands are estimated as 26.5, 26.1, 25.9, 25.1, and 24.4, respectively (Uchiyama et al. 2022).

(viii) *Count the number of possible quasar objects:* We utilize the enhanced image $\mathcal{D}_{\rm shp}$ to improve the identification of point sources and to obtain more reliable PSF magnitudes than those in the HSC catalogue (see Fig. 4). With the new flux measurements obtained in Step (vi), we apply the quasar *grizy* colour cuts as used in our preselection method (see equation 1) to eliminate quasars contaminated by nearby stars or galaxies. When a system contains multiple potential quasar objects, we group them based on their colour differences, defined as:

$$|\Delta \boldsymbol{c}|^2 = \left|\boldsymbol{c}_i - \boldsymbol{c}_j\right|^2 < 1, \tag{7}$$

where $\boldsymbol{c}$ is the colour vector for each object, given as $\boldsymbol{c} = (g - r, r - i, i - z, z - y)$, and i and j are the indices of the two objects being compared. For simplicity, here we assign equal weight to the colour difference. The number of possible quasar objects (dubbed as possible lensed images) in each group is counted as $n_{\rm img}$. We proceed to the next step for systems with at least one group containing $2 \leq n_{\rm img} \leq 5$ possible lensed images. The upper limit of $n_{\rm img} = 5$ is empirically chosen to reduce contamination from dense star-forming galaxies or high-density stellar fields. We note that sometimes a quasar image can fall outside of the colour cuts, for example when a quasar is contaminated by the light of its lensing galaxy or is at a high redshift, as seen in examples such as B1600+434 and SDSSJ1452+4224 in Fig. 5. While relaxing the quasar colour cuts could prevent such cases, it would also increase the likelihood of false detections.

[1]We set the threshold to 30 `std`, where `std` is estimated using `sigma_clipped_stats`. The other parameters of `DAOStarFinder` are set to default values.

Table 2. Lensed quasar selection efficiency for different catalogues. 'Algorithm' is indicated for our classification method in Section 3, 'Phase 1' is denoted for the visual binary classification, and $G_{\rm av}$ is the average grade from the grading visual inspection. The percentage is relative to the 'Input' number. The numbers include the known lensed quasars. 'Total' in the last row provides an assessment of the overall performance, after cross-matching the three catalogues within a 2 arcsec radius.

Catalogue	Input	Algorithm	(per cent)	Phase 1	(per cent)	$G_{\rm av} \geq 2$	(per cent)
HSC + unWISE	1 587 892	121 511	7.65	6111	0.38	162	0.010
MILLIQUAS	150 316	1368	0.91	376	0.25	38	0.025
AllWISEAGN	49 943	438	0.88	117	0.23	22	0.044
Total	1 652 329	121 880	7.38	6199	0.38	162	0.010

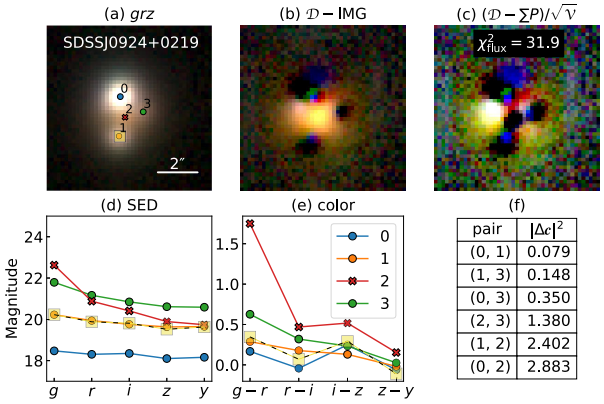

Figure 4. Output of the classification method on the known lens SDSSJ0924+0219: (a) composite image in the HSC *grz* bands, (b) residuals upon subtraction of point sources in quasar group, (c) normalized residuals upon subtraction of the detected point sources, (d) SED of the detected point sources, (e) colour of the detected point sources, and (f) table of colour difference. Circles and crosses indicate the positions of quasar and non-quasar point sources, respectively. The positions and photometry from the HSC catalogue are represented in yellow squares.

(ix) *Classify as a lens candidate:* In order to reduce the number of false positives, we introduce three additional thresholds. First, we require the maximum magnitude difference between multiple point sources in each filter to be $\Delta m < 2$, since large flux ratios are not compatible with lens models and not observed in known lenses (see fig. 3 in Chan et al. 2022). Secondly, lensing galaxies are typically fainter than quasar images, and even though their light can be prominent, the outskirt contribution is often insignificant after subtracting the central bulges [which we do using PSF fitting in Step (vi)]. Therefore, we adopt a residual flux fit threshold of $\chi^2_{\rm flux} < 200$. Thirdly, thanks to the high image quality of HSC, we impose an image separation (sep.) of <3 arcsec and aim to expand the lens sample size in this regime.

We calibrate this method using a sample of optically bright known lensed quasars with HSC DR4 imaging, compiled in the Gravitationally Lensed Quasar Database (GLQD; Lemon et al. 2022).[2] We recover 18 of 22, resulting in a recovery rate of 80 per cent, via colour-cut preselection and the classification algorithm: $2 \leq n_{\rm img} \leq 5$, $\Delta m < 2$, sep. < 3 arcsec, and $\chi^2_{\rm flux} < 200$. The results are shown in Table 3 and Fig. 5. We note that the measurements in the HSC catalogue can be blended, leading to ambiguity in separating lensed quasar images and lensing galaxies (illustrated as yellow squares and pink crosses in Fig. 5). This test demonstrates as well our improved ability to disentangle multiple components within a lens system. The four failures are listed as below:

(i) J0941+0518: wide image separation ≈6 arcsec;
(ii) B1600+434: slightly off quasar colour in image 1, due to lensing galaxy light;
(iii) BRI0952−0115: high redshift quasar mis-classified by the colour-cut selection ($z = 4.5$);
(iv) SDSSJ1452+4224: high redshift quasar mis-classified by the colour-cut selection ($z = 4.8$).

After performing calibration on the method, we then apply to the preselected quasar candidates from Section 2, resulting in a reduced sample size of 121 511 systems (7.4 per cent) for visual inspection. This represents a significant reduction from the original catalogue size. The computational time for analysing each system is approximately 2 s.

4 VISUAL INSPECTION

To handle the large number of lens candidates (121 511), we propose a two-phase visual inspection process. In this process, we intentionally include quasar pairs as candidates because they are a byproduct of this work and can provide valuable insights into the existence of supermassive black hole pairs and galaxy mergers in the early Universe (e.g. Goulding et al. 2019; Casey-Clyde et al. 2021). During the first phase of visual inspection, we perform a binary classification of 'possible lens or quasar pair' and 'other', which is carried out by the first three authors. JHHC inspects the whole sample, while KCW and XD share it equally, ensuring that each system is reviewed by two independent inspectors. At this stage we take a conservative approach, focusing on maintaining possible lenses or quasar pairs. Nevertheless, we ensure to remove any apparent non-target objects that could lead to false positives. Each system's image for inspection is generated from the results of the classification algorithm, as shown in Fig. 4. To better identify faint, compact lensing galaxies, we take residual images obtained by subtracting the possible lensed images. The majority of candidates are classified as 'other' in this phase due to one or several of the following reasons:

(i) saturated pixels in the cutout, as they can produce false point source detections in our algorithm, especially in the existing catalogues;
(ii) obvious extended galaxies or non-point sources in the images, such as the host galaxy of a low-redshift AGN or a galaxy merger.

Each case is illustrated in Fig. 6. By taking the union of the three sets from the first three inspectors, we identify 6199 candidates for the next phase.

[2]GLQD: https://research.ast.cam.ac.uk/lensedquasars/index.html

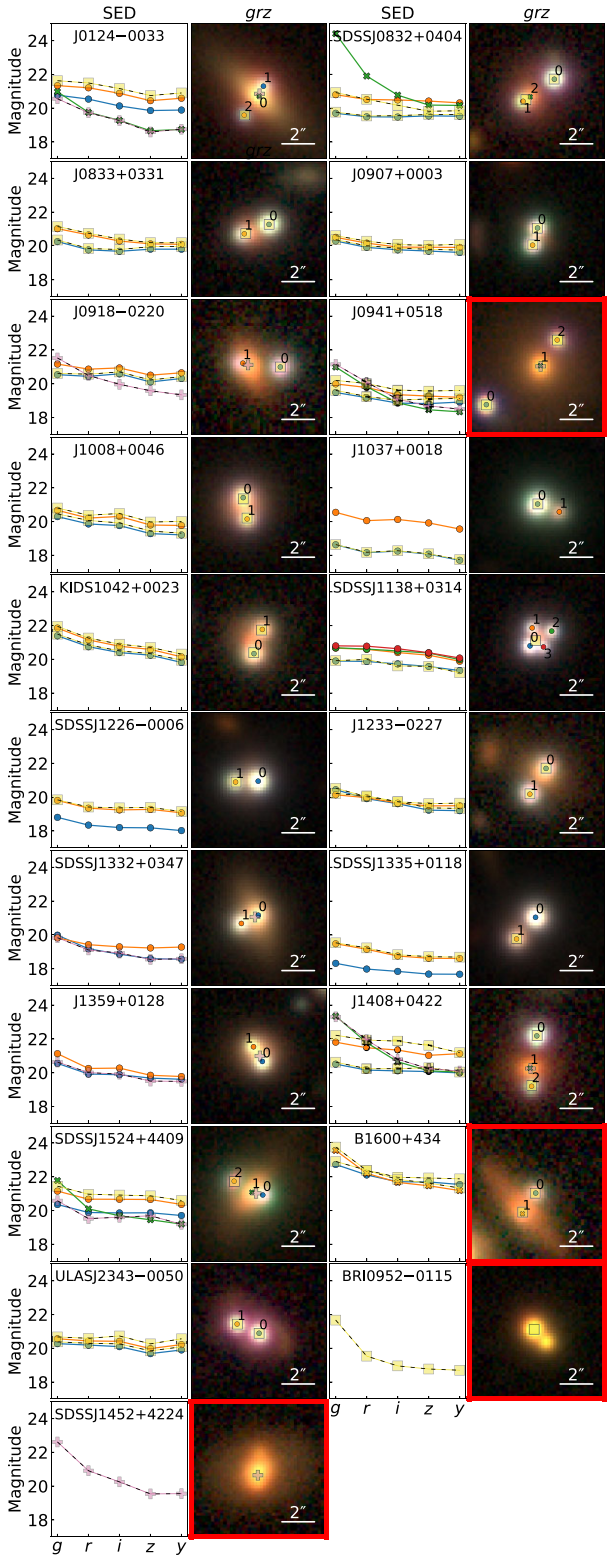

Figure 5. Known lens test for the classification method. The labels are same as Figs 4(a) and (d). The measurements from the HSC catalogue are denoted in yellow squares and pink crosses, representing two components of a lens system: lensed quasar image and lensing galaxy, respectively. The lenses which are not able to be recovered are highlighted with the red frames. BRI0952−0115 and SDSSJ1452+4224 fail the colour-cut preselection due to high redshift quasars. J0941+0518 has a wide image separation ≈6 arcsec, while B1600+434 exhibits an image with slightly off quasar colour due to lens light contamination.

Table 3. Summary of the known lensed quasars.

Name	RA (deg)	Dec. (deg)	$n_{\rm img}$	$G_{\rm av}$	Ref.
J0124−0033	21.2394	−0.5533	2	3.0	[11]
SDSSJ0832+0404	128.0710	4.0679	2	2.5	[6]
J0833+0331	128.3369	3.5247	2	2.5	[13]
J0907+0003	136.7937	0.0559	2	3.0	[14]
J0918−0220	139.6806	−2.3354	2	2.5	[12]
SDSSJ0924+0219	141.2325	2.3236	3	2.5	[3]
J0941+0518	145.3439	5.3066	2	–	[10]
J1008+0046	152.1932	0.7724	2	3.0	[13]
J1037+0018	159.3665	0.3057	2	2.5	[13]
KIDS1042+0023	160.6553	0.3839	2	3.0	[14]
SDSSJ1138+0314	174.5155	3.2494	4	3.0	[7]
SDSSJ1226−0006	186.5334	−0.1006	2	2.5	[7]
J1233−0227	188.4219	−2.4604	2	3.0	[13]
SDSSJ1332+0347	203.0942	3.7944	2	2.0	[5]
SDSSJ1335+0118	203.8950	1.3015	2	2.5	[4]
J1359+0128	209.9342	1.4693	2	3.0	[12]
J1408+0422	212.1406	4.3747	2	3.0	[13]
SDSSJ1524+4409	231.1901	44.1638	2	3.0	[6]
B1600+434	240.4185	43.2799	1	–	[2]
ULASJ2343−0050	355.7998	−0.8429	2	2.0	[8]
BRI0952−0115	148.7504	−1.5019	–	–	[1]
SDSSJ1452+4224	223.0479	42.4082	–	–	[9]

Note. [1] McMahon, Irwin & Hazard (1992), [2] Jackson et al. (1995), [3] Inada et al. (2003), [4] Oguri et al. (2004), [5] Morokuma et al. (2007), [6] Oguri et al. (2008), [7] Inada et al. (2008), [8] Jackson, Ofek & Oguri (2008), [9] More et al. (2016), [10] Williams et al. (2018), [11] Lemon et al. (2019), [12] Jaelani et al. (2021), [13] Lemon et al. (2022), and [14] GLQD.

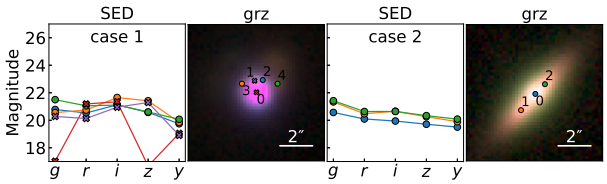

Figure 6. Examples of objects classified as 'other' during the visual binary classification, due to bad pixels (case 1), and extended galaxies (case 2).

The second phase involves a quaternary classification in which each inspector grades candidates from 0 to 3 using only integer values, according to the following criteria:

3: very likely to be a lens, requiring resolved spectroscopy for confirmation;

2: blue point sources at modest separation with similar quasar-like colours and without an obvious lensing galaxy;

1: same as the previous grade but with slightly high values of PMSIG and AEN (definitions explained later in this section), as well as larger differences in colours;

0: a system that likely contains a star, star-forming galaxy, or a very low-redshift quasar.

To avoid bias, we assign each system two grades. First, JHHC goes through the entire sample and divides it into nine batches, which are shared by JHHC, KCW, DC, IC, ATJ, IK, AM, MO, and SHS. JHHC grades some candidates twice to check grade consistency. For each candidate, we inspect any relevant data of the system, including SDSS images and spectra, DECaLS images[3] (Dey et al. 2019), unWISE images (Meisner, Lang & Schlegel 2018), catalogues

[3]DECaLS: https://www.legacysurvey.org

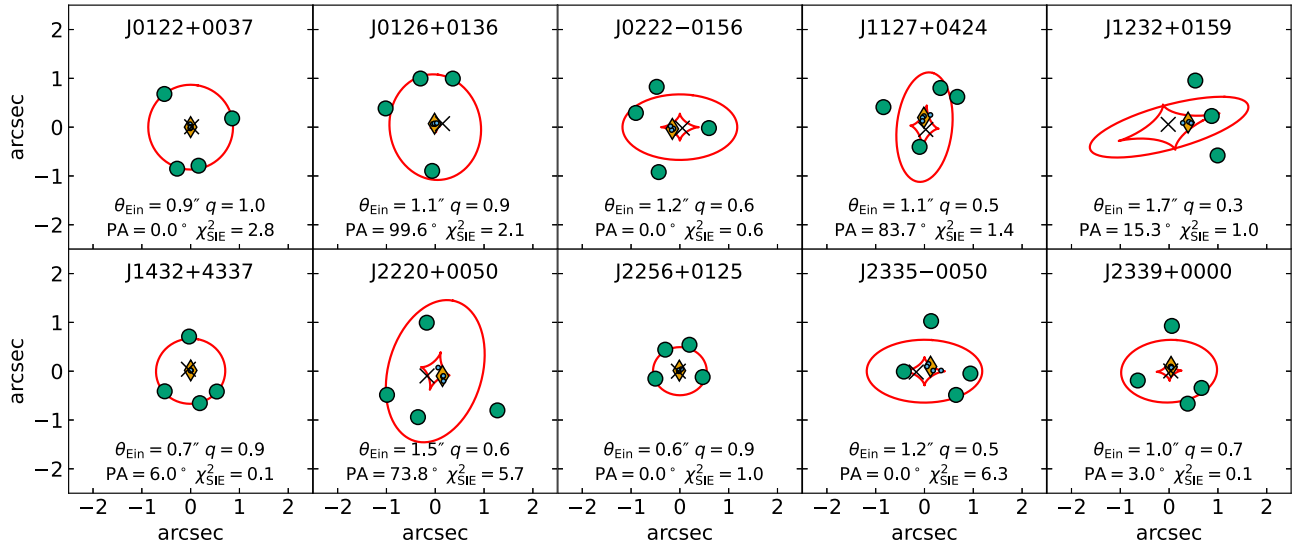

Figure 7. Lens modelling for quadruply lensed quasar candidates. A set of model parameters are denoted at the bottom of each panel, and the resulting critical curves and caustics are illustrated in red lines. The galaxy position is obtained from light modelling, represented as black cross. The lensed image positions obtained from light modelling are shown as green circles, while the mapped sources are represented by blue dots. The modelled source position is labelled as orange diamonds.

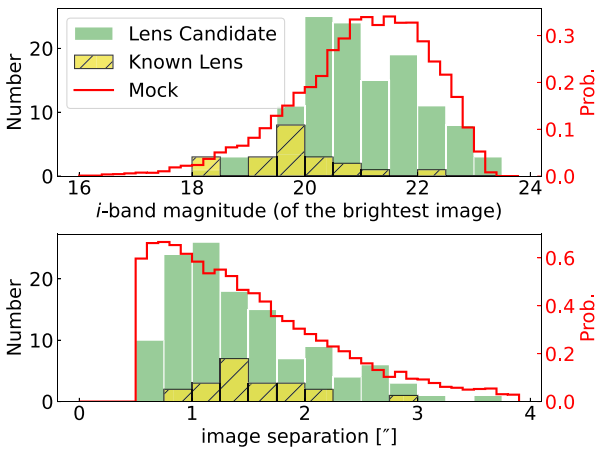

Figure 8. Histograms of the *i*-band magnitude (top) and of the image separation (bottom). The *i*-band magnitude and image separation are obtained from the brightest putative lensed images and the maximum distance between them, respectively. The photometry and astrometry of lens candidates (green) are measured from light modelling and those of known lenses (yellow) are from the classification algorithm. The probability distributions of our lens candidates are consistent with those of the mocks (red) in Oguri & Marshall (2010).

of VizieR (Ochsenbein, Bauer & Marcout 2000), NED,[4] and Simbad (Wenger et al. 2000). We also consider *Gaia* DR3 proper motions (converted to the PMSIG parameter defined in Lemon et al. 2019), and astrometric excess noise (AEN; Gaia Collaboration 2016, 2022). A large PMSIG value ($\gtrsim$10 σ) strongly suggests that the system contains a star, while a high AEN value ($\gtrsim$10 mas) may indicate a candidate star-forming galaxy (see figs 1 and 2 in Lemon et al. 2019). We acknowledge that the grading process is subjective and time-consuming, and we note that only JHHC has seen images of confirmed lensed quasars. While the two grades assigned to each system are usually nearly identical, there are cases where there is a grade difference ($\Delta G \geq 2$), likely due to personal grading experience or human fatigue. After discussing these candidates, the percentage of cases with $\Delta G \geq 2$ drops from 7 per cent to <3 per cent. In the end, we take the average of the two grades assigned to each system ($G_{\rm av}$), resulting in 31 systems with $G_{\rm av} = 3$, 42 systems with $G_{\rm av} = 2.5$, and 89 systems with $G_{\rm av} = 2$. We then perform detailed modelling for a total of 162 candidates in Section 5.

[4]The NASA/IPAC Extragalactic Database (NED) is operated by the Jet Propulsion Laboratory, California Institute of Technology, under contract with the National Aeronautics and Space Administration.

5 LIGHT AND LENS MODELLING ANALYSIS

A lensed quasar system is expected to have a lensing galaxy that is surrounded by multiple lensed images of the quasar. However, in most cases, the lensing galaxy is much fainter than the quasar and can hardly be seen in ground-based imaging. Although our classification method is effective at highlighting lensing galaxies by removing lensed quasar images (as demonstrated in Fig. 4), double point sources can sometimes remain, creating a residual that mimics a lensing galaxy. To tackle this issue, we aim to optimally subtract any discernible point sources (or single point sources and galaxies), to enhance our ability to identify a lensing galaxy or counter image in the deep, high-resolution HSC imaging. This approach is applied to the most promising 162 systems resulting from our visual inspection.

We model point sources using a Moffat profile [from Step (i) in Section 3] and galaxies using a Sérsic profile (Sérsic 1963). We manually determine the numbers of point sources ($N_{\rm PS}$) and galaxies ($N_{\rm GAL}$) for each system, and simultaneously fit the *grizy* bands. The resulting χ^2 is defined as

$$\chi^2_{\rm light} = \frac{1}{N_{\rm band} \cdot N_{\rm pix}} \sum_{grizy} \sum_{i,j} \frac{[\mathcal{D}(i,j) - \mathcal{M}(i,j)]^2}{\mathcal{V}(i,j)}. \quad (8)$$

The model image $\mathcal{M}$ is the sum of all components in each band:

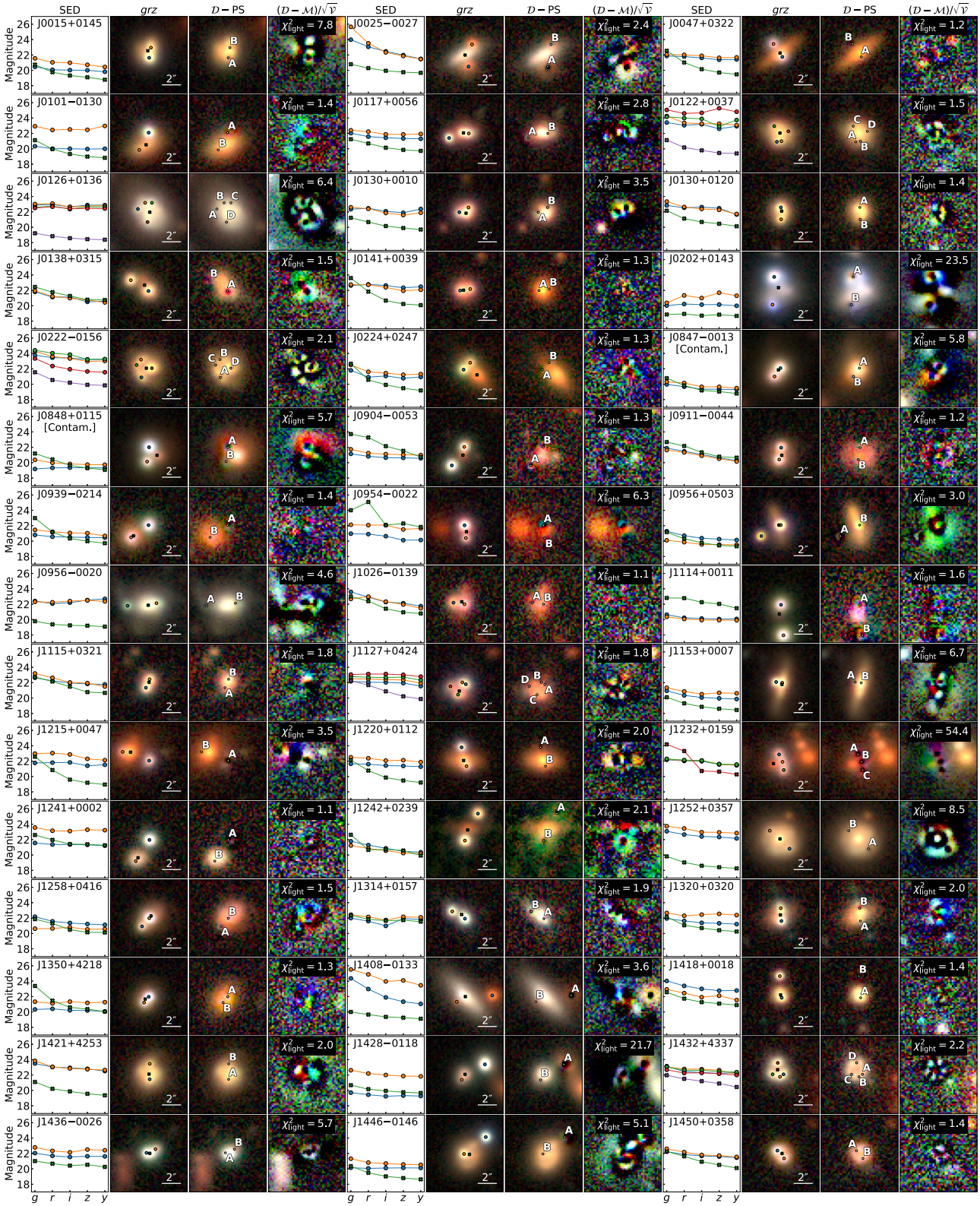

Figure 9. Lensed candidates classified as grade A. Each candidate contains 'SED', '*grz*', '$\mathcal{D}-$PS', and '$(\mathcal{D}-\mathcal{M})/\sqrt{\mathcal{V}}$' from light modelling. The labels in 'SED' and '*grz*' are the same as Figs 4(a) and (d). The results of light modelling for each component are listed in Table B1. The contaminants are noted under their names.

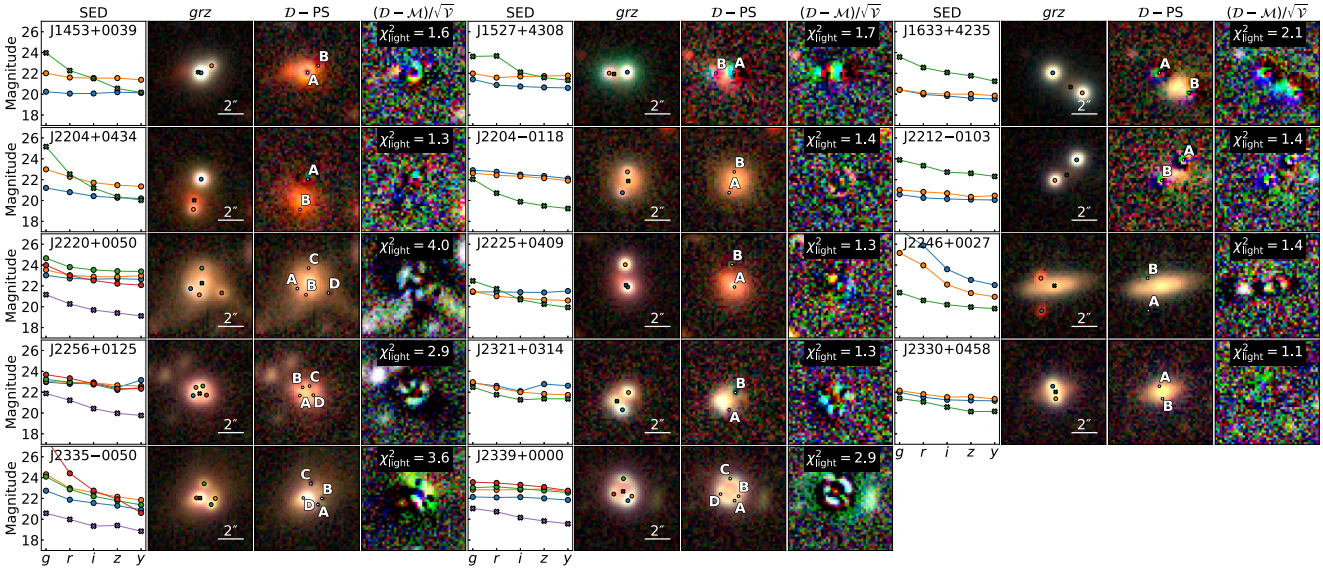

Figure 9. *– continued*

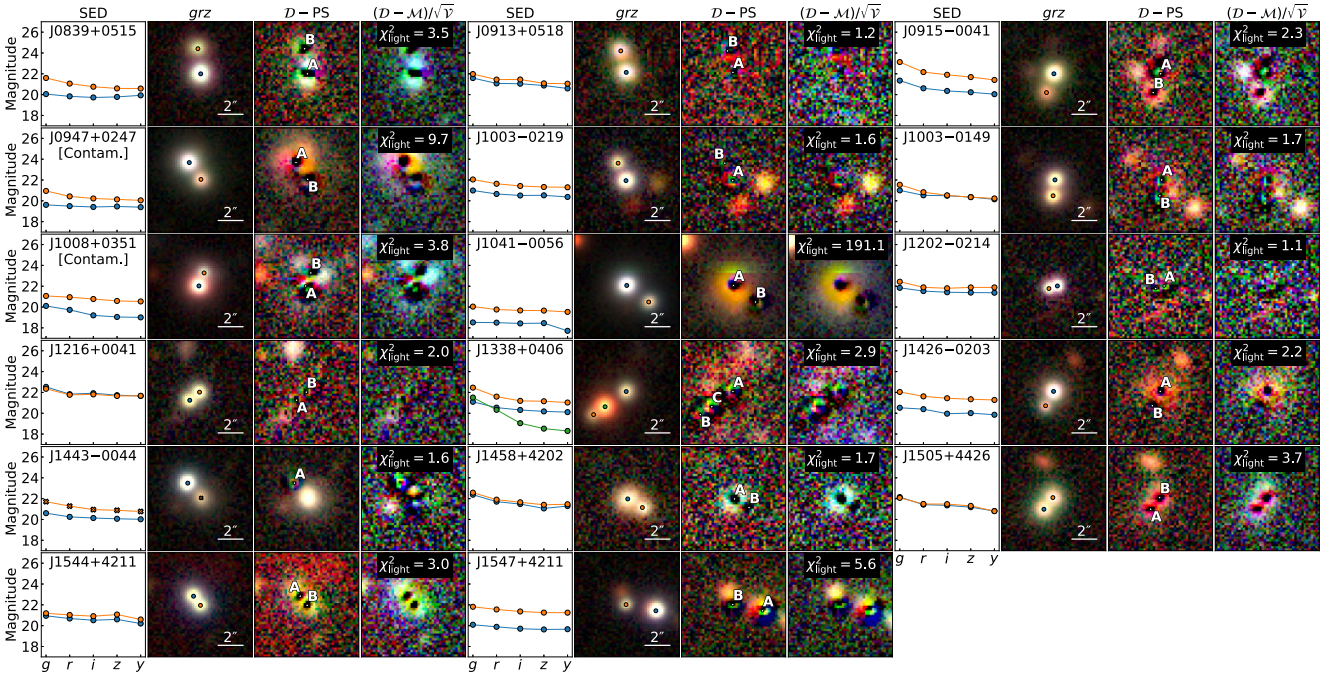

Figure 10. Lensed candidates classified as grade B. The labels are the same as Fig. 9.

$$\mathcal{M} = \sum_{k}^{N_{\rm PS}} P_k(\boldsymbol{r}_{p,k}) + \sum_{k}^{N_{\rm GAL}} S_k(A_k, R_{e,k}, e_k, \phi_k, n_k, \boldsymbol{r}_{l,k}), \tag{9}$$

where k is the index of each component, P is the scaled Moffat PSF at the position parameter $\boldsymbol{r}_p$, and S is a scaled Sérsic profile with the parameters of the intensity (A), the effective radius ($R_{\rm e}$), the ellipticity (e), the orientation (ϕ), the Sérsic index (n), and the centre ($\boldsymbol{r}_l$). The results of the light modelling can be found at the end of the paper (see Figs 9–11). The measured astrometry and photometry are listed in Table B1.

We consider a few candidates with the potential to contain quadruply lensed images, and model their image configuration using a singular isothermal elliptical (SIE) lens mass distribution. This involves using parameters such as the Einstein radius ($\theta_{\rm Ein}$), axis ratio (q), position angle (PA), and lens centre ($\boldsymbol{r}_{\rm SIE}$). The resulting χ^2 is calculated by comparing the modelled and observed source positions, as well as by comparing the lens mass to light centres (Oguri 2010; Chan et al. 2015, 2020), which can be described as:

$$\chi^2_{\rm SIE} = \sum_{k} \frac{\mu_k \left|\boldsymbol{\beta}_k - \boldsymbol{\beta}_{\rm SIE}\right|^2}{{\sigma_k}^2} + \frac{|\boldsymbol{r}_{\rm SIE} - \boldsymbol{r}_l|^2}{{\sigma_l}^2}, \tag{10}$$

where $\boldsymbol{\beta}_k$ is the respective source position mapped from the position of lensed image k with the magnification μ_k, and $\boldsymbol{\beta}_{\rm SIE}$ is the modelled

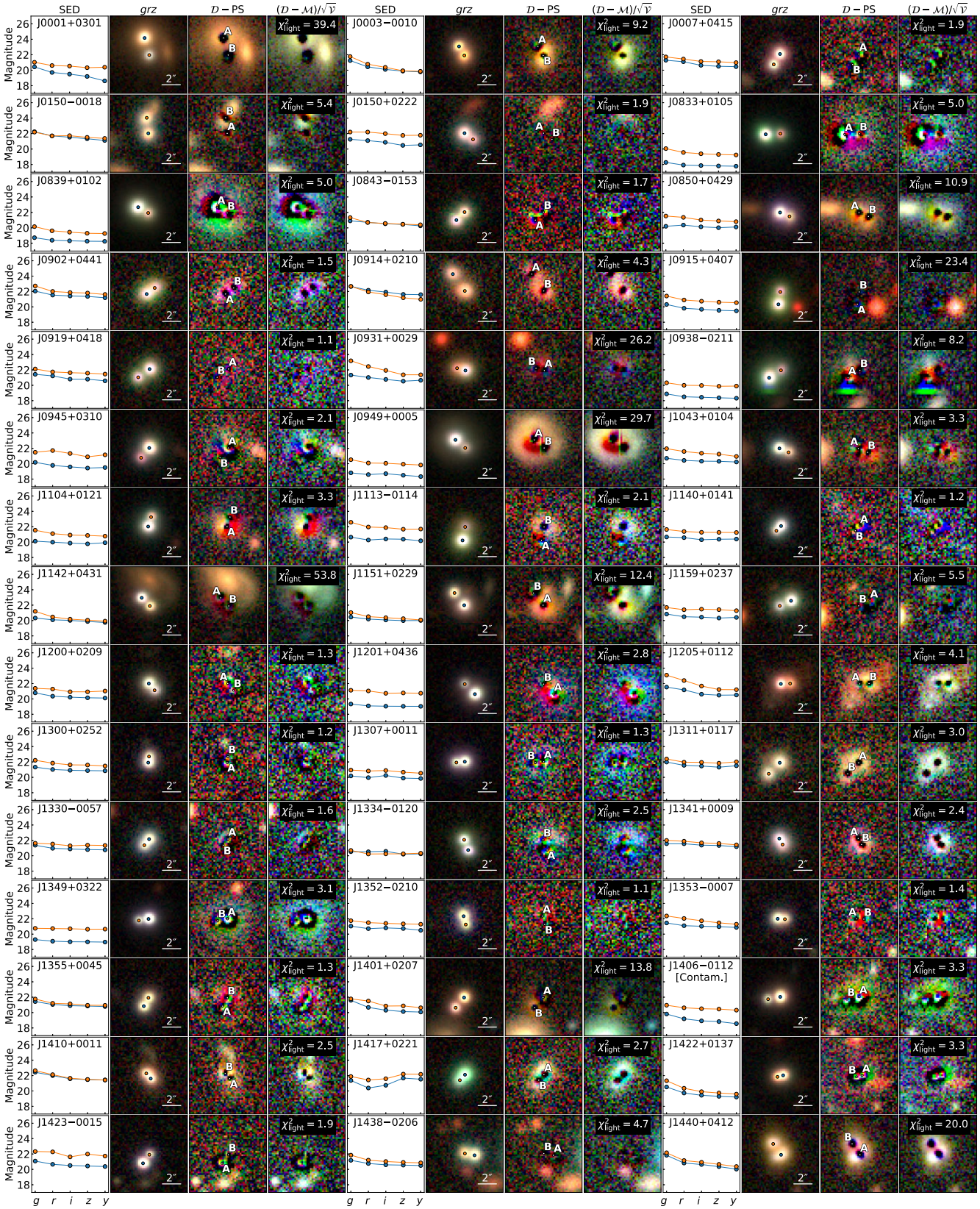

Figure 11. Lensed candidates classified as grade C. The labels are the same as Fig. 9.

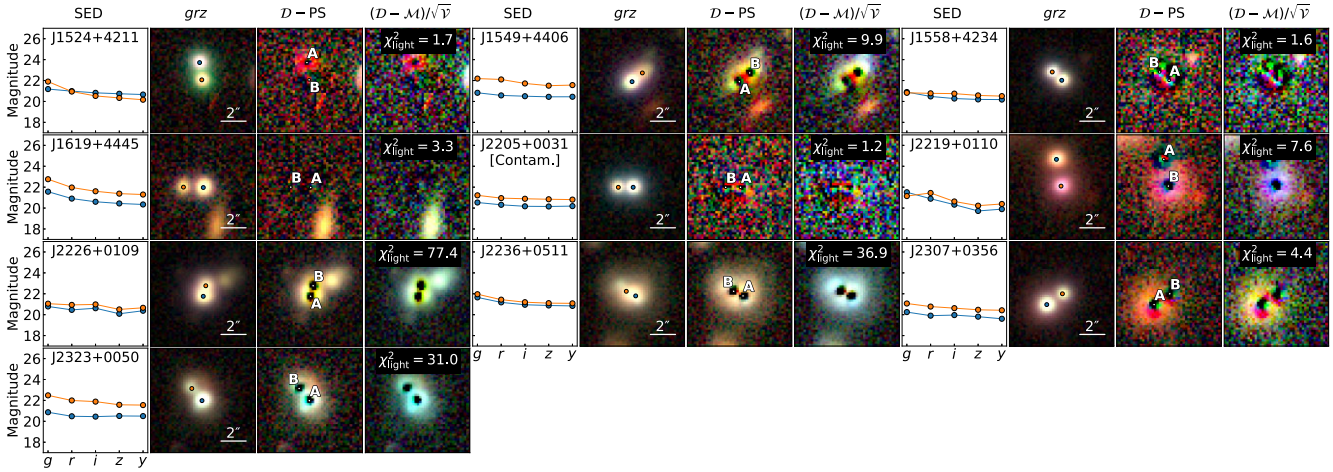

Figure 11. – *continued*

source position evaluated as a weighted mean of $\boldsymbol{\beta}_k$,

$$\boldsymbol{\beta}_{\rm SIE} = \frac{\sum_k \sqrt{\mu_k} \cdot \boldsymbol{\beta}_k}{\sum_k \sqrt{\mu_k}}. \tag{11}$$

The light centre $\boldsymbol{r}_l$ is obtained from the light modelling, with the uncertainties of image and lens positions conservatively to be the pixel scale of HSC, i.e. $\sigma_k = \sigma_l = 1$ pix $= 0.168$ arcsec. Although this choice does not affect the fit, we adopt it for consistency. The lens modelling results are illustrated in Fig. 7.

6 RESULT

According to modelling results on 162 candidates with $G_{\rm av} \geq 2$, we provide the final grades as:

A requiring a fit with at least two point sources and one galaxy;
B not satisfying A but with $G_{\rm av} > 2$;
C not satisfying A but with $G_{\rm av} = 2$;
G likely to be a lensed galaxy.

The results are summarized in Tables 4–6, which include the maximum distance between point sources as a tentative measure of image separation. We should note that in some cases, determining whether a source is best modelled as a point source or/and a Sérsic profile can be ambiguous, particularly for compact sources. There are ten candidates identified as potentially containing quadruply lensed images (quads), with six showing promising results and four being inconclusive. A specific classification, referred as grade G, is described in Appendix A, indicating the likely presence of arcs after single galaxy fit. We also find candidates with two widely separated point sources without a galaxy in between, which are not lenses but may be quasar pairs or nearly identical quasars. These have potential applications in black hole science. The number of such candidates with $G_{\rm av} < 2$ is 774, which are not presented in this work but may be made available upon request from the authors.

Only 60 per cent of the quasars in the existing catalogues are identified in the catalogue using colour cuts. However, according to our findings, the colour-cut preselection is comprehensive as it includes all candidates with $G_{\rm av} \geq 2$. While existing quasar catalogues can lead to higher classification efficiency (see Table 2), our results demonstrate the effectiveness of photometric selection for lensed quasar searches, especially when considering *WISE* colours.

The high-resolution and deep imaging capabilities of HSC enable us to expand the sample size of low-brightness and small-image-separation lenses. Although we have yet to confirm the nature of our candidates, we present histograms of the lens candidate sample as a function of the *i*-band magnitude of the brightest image and the putative image separation in Fig. 8. These probability trends closely follow those seen in the mock catalogue simulations (Oguri & Marshall 2010), providing further support for the validity of our method.

We provide individual notes for several interesting systems, such as potential quads, grade A candidates with spectroscopic redshifts, and those with identified contaminants, although the list is not comprehensive.

6.1 J0122+0037 (quad)

This system is a promising lens, though the lensed images do not appear as point sources. We conducted a tentative fit using four point sources and one galaxy and find that the image configuration can be well modelled with an SIE. However, an SIE with $q = 1$ is less likely to produce a quad system, possibly due to the poor representation of the lensed arc feature using four point sources. Further confirmation of its nature will require high-resolution imaging or spectroscopy.

6.2 J0126+0136 (inconclusive)

This system could be a lensed galaxy. We tentatively fit with four point sources and one galaxy, but the lensing feature is not clearly pronounced. Therefore, we note it as inconclusive.

6.3 J0222−0156 (inconclusive)

We performed a tentative fit for this system using four point sources and one galaxy. Although the lens model can fit the data, we observed that the lensing feature of components A, B, and C could also be formed by two galaxies, as shown in the residual. Additionally, the galaxy fit at the centre is not consistent with the light modelling, indicating that the results are not promising. Therefore, we consider this system to be inconclusive.

6.4 J1127+0424 (quad)

This system exhibits a clear fold configuration, with two adjacent images close to the critical curve, and can be well modelled by an

Table 4. Lensed candidates classified as grade A. The preselected quasar catalogues are denoted as 'MQ' for MILLIQUAS, 'AW' for AllWISEAGN, and 'HW' for colour-cut selection using the HSC + unWISE photometry. The average grades of the visual inspection are listed as $G_{\rm av}$. The image separation is measured via light modelling. The references and grades in 'comment' are determined in the previous lens search works using the DECaLS data. The candidates as potential quads are highlighted with † sign following their 'Name' and the confirmed contaminants are denoted in 'Comment'.

Name	RA (deg)	Dec. (deg)	Catalogue	$G_{\rm av}$	Sep. (arcsec)	Comment
HSC J0015+0145	3.786619	1.754679	HW	2.0	1.010	
HSC J0025−0027	6.253408	−0.456018	HW	3.0	2.204	
HSC J0047+0322	11.912319	3.375557	HW	3.0	1.542	[3]: grade A
HSC J0101−0130	15.290820	−1.501892	HW	2.0	1.927	
HSC J0117+0056	19.481317	0.944474	HW	2.5	1.988	
HSC J0122+0037†	20.682424	0.626798	HW	2.5	1.628	
HSC J0126+0136†	21.688665	1.614272	HW	2.0	1.939	
HSC J0130+0010	22.562941	0.183304	HW	2.0	1.021	
HSC J0130+0120	22.642658	1.343466	HW	2.0	1.168	
HSC J0138+0315	24.613569	3.255110	HW	3.0	2.032	
HSC J0141+0039	25.468628	0.665588	MQ, HW	3.0	1.007	
HSC J0202+0143	30.714681	1.722141	HW	2.0	2.725	
HSC J0222−0156†	35.719655	−1.947280	HW	3.0	1.747	
HSC J0224+0247	36.076293	2.784369	HW	2.5	0.941	
HSC J0847−0013	131.793355	−0.217367	MQ, HW	3.0	1.008	Contam.; [2]: grade C
HSC J0848+0115	132.233697	1.261151	AW, MQ, HW	2.5	1.422	Contam.
HSC J0904−0053	136.143646	−0.891211	HW	3.0	2.193	[1]: grade C
HSC J0911−0044	137.964866	−0.735081	HW	2.5	1.180	
HSC J0939−0214	144.968377	−2.233758	HW	2.5	2.081	
HSC J0954−0022	148.529041	−0.373677	MQ, HW	2.5	1.261	
HSC J0956+0503	149.056324	5.057322	HW	2.0	2.190	
HSC J0956−0020	149.247607	−0.343281	HW	2.0	2.853	
HSC J1026−0139	156.639280	−1.657137	HW	2.5	1.090	
HSC J1114+0011	168.730641	0.187346	HW	2.5	3.013	
HSC J1115+0321	168.967523	3.359870	HW	2.0	0.914	
HSC J1127+0424†	171.990419	4.403943	HW	2.5	1.528	
HSC J1153+0007	178.394009	0.128271	HW	2.0	0.606	
HSC J1215+0047	183.767960	0.790340	HW	3.0	2.746	
HSC J1220+0112	185.078965	1.214970	HW	3.0	1.917	
HSC J1232+0159†	188.048666	1.992294	HW	2.5	1.601	
HSC J1241+0002	190.269856	0.048677	HW	2.5	2.471	
HSC J1242+0239	190.698372	2.665997	HW	2.5	2.941	
HSC J1252+0357	193.091405	3.964250	HW	3.0	2.630	
HSC J1258+0416	194.585101	4.271747	HW	2.5	1.078	
HSC J1314+0157	198.661028	1.954338	HW	3.0	1.433	
HSC J1320+0320	200.185492	3.345479	HW	2.0	1.255	
HSC J1350+4218	207.734398	42.303871	AW, MQ, HW	2.5	0.729	
HSC J1408−0133	212.160912	−1.561510	HW	2.0	3.539	
HSC J1418+0018	214.626884	0.300308	HW	2.5	2.131	
HSC J1421+4253	215.457752	42.897449	HW	2.0	1.516	
HSC J1428−0118	217.114641	−1.313045	HW	2.0	2.739	
HSC J1432+4337†	218.190248	43.626438	HW	3.0	1.382	
HSC J1436−0026	219.007587	−0.444933	MQ, HW	2.5	0.959	
HSC J1446−0146	221.676431	−1.783056	HW	2.0	2.706	
HSC J1450+0358	222.668927	3.967973	HW	2.0	1.006	
HSC J1453+0039	223.447798	0.657522	MQ, HW	2.0	0.924	
HSC J1527+4308	231.966601	43.133721	HW	3.0	1.316	
HSC J1633+4235	248.320266	42.589050	HW	2.0	2.586	
HSC J2204+0434	331.021369	4.581936	HW	3.0	2.261	
HSC J2204−0118	331.239563	−1.308067	HW	2.5	1.558	
HSC J2212−0103	333.069234	−1.062676	MQ, HW	2.0	2.173	
HSC J2220+0050†	335.115248	0.838401	HW	2.5	2.307	
HSC J2225+0409	336.484637	4.160303	HW	2.5	1.627	
HSC J2246+0027	341.623573	0.458973	HW	2.0	2.352	
HSC J2256+0125†	344.031107	1.426382	HW	2.5	0.985	
HSC J2321+0314	350.485037	3.245266	HW	3.0	1.329	
HSC J2330+0458	352.572135	4.979310	HW	3.0	0.933	
HSC J2335−0050†	353.993383	−0.833345	AW, MQ, HW	3.0	1.597	
HSC J2339+0000†	354.921476	0.012083	HW	3.0	1.626	[3]: grade A

Note. [1] He et al. (2023), [2] Dawes et al. (2022), and [3] Storfer et al. (2022).

Table 5. Lensed candidates classified as grade B. The notations are the same as Table 4.

Name	RA (deg)	Dec. (deg)	Catalogue	G_{av}	Sep. (arcsec)	Comment
HSC J0839+0515	129.781060	5.264559	HW	2.5	1.836	
HSC J0913+0518	138.316230	5.311164	HW	2.5	1.609	
HSC J0915−0041	138.861961	−0.693524	HW	2.5	1.468	
HSC J0947+0247	146.804584	2.795174	AW, MQ, HW	2.5	1.486	Contam.
HSC J1003−0219	150.954982	−2.318416	HW	3.0	1.390	
HSC J1003−0149	150.993709	−1.831603	HW	2.5	1.160	
HSC J1008+0351	152.248168	3.851162	AW, MQ, HW	2.5	1.016	Contam.
HSC J1041−0056	160.345191	−0.938461	AW, MQ, HW	2.5	1.997	
HSC J1202−0214	180.740787	−2.242944	HW	2.5	0.641	
HSC J1216+0041	184.218605	0.686800	HW	2.5	0.922	
HSC J1338+0406	204.705584	4.107964	HW	3.0	2.901	
HSC J1426−0203	216.748160	−2.064914	HW	2.5	1.191	
HSC J1443−0044	220.780108	−0.741738	HW	3.0	–	
HSC J1458+4202	224.619091	42.039571	HW	2.5	1.232	
HSC J1505+4426	226.398343	44.434654	HW	2.5	1.069	
HSC J1544+4211	236.095224	42.198152	HW	2.5	0.834	
HSC J1547+4211	236.989002	42.189374	HW	2.5	2.211	

Note. [1] He et al. (2023), [2] Dawes et al. (2022), and [3] Storfer et al. (2022).

SIE. However, further confirmation of its nature will require high-resolution imaging or spectral data.

6.5 J1232+0159 (quad)

This system contains a triplet of lensed images with the same colour, although the fourth image is difficult to detect. We model the three lensed images and find that the lens model is highly elliptical, likely due to the nearby galaxy group (see Fig. 9). High-resolution imaging or spectroscopic observations are needed to confirm the nature of this system.

6.6 J1432+4337 (quad)

This system is a promising lens, although the lensed images do not appear to be point sources, and there is a possibility that they may be blended with lensed arcs.

6.7 J2220+0050 (inconclusive)

This system has a galaxy spectrum with a redshift of $z = 0.616$ obtained from VVDS.[5] However, the image D appears slightly reddened and out of position, leading to a larger $\chi^2_{\rm SIE}$. Therefore, we classify this system as inconclusive.

6.8 J2256+0125 (inconclusive)

Thanks to the HSC image quality, we can see a small arc in this system. We tentatively fit with four point sources and one galaxy, though image D is hardly detected. Due to its small image separation around 1 arcsec, we note it as inconclusive.

6.9 J2335−0050 (quad)

This system is identified as a type 2 Seyfert galaxy at redshift $z = 0.438$ based on the SDSS spectrum. However, the fourth image (image D) is unclear and not visible in the HSC images. If it turns out to be a lens, we note that there is a strong flux anomaly between images A and B.

[5]VVDS: https://cesam.lam.fr/vvds/

6.10 J2339+0000 (quad)

This system has clear lensing features, including a fold configuration and visible lensed arcs in the residuals. High-resolution imaging and/or a spectrum are needed to confirm the nature of the source.

6.11 J1338+0405 (inconclusive)

This system appears to be a doubly lensed quasar, but the identification of image C as a star with a large PMSIG = 36.7 σ creates uncertainty. Therefore, we note this system as inconclusive.

6.12 J0141+0039 (double)

This system has been confirmed as a quasar source with redshift $z = 2.198$ in SDSS, and it has been identified as a strong candidate for a gravitational lens in SQLS. Although follow-up spectroscopic observations have been conducted, its status as a lensed quasar remains uncertain due to its small separation of only about 1 arcsec.

6.13 J0954−0022 (double)

This system has been confirmed as a quasar source with a redshift of $z = 2.267$ using the 2dF instrument on the Anglo-Australian Telescope. Based on our light modelling, we estimate the image separation to be 1.26 arcsec. However, the lensing galaxy is obscured, making it difficult to study the lensing properties in detail.

6.14 J1436−0026 (inconclusive)

This system is confirmed as a quasar at redshift $z = 0.5615$ in the 2SLAQ catalogue (Croom et al. 2009). However the galaxy fit is unclear, as it appears to be brighter than the other two point sources. Therefore, we note it as inconclusive until further observations can provide more information.

6.15 J1453+0039 (inconclusive)

This system is confirmed as a quasar at redshift $z = 1.094$ from SDSS. However, the galaxy fit appears to be slightly displaced from the expected position, which may be due to the presence of a nearby galaxy. As a result, we note it as inconclusive.

Table 6. Lensed candidates classified as grade C. The notations are the same as Table 4.

Name	RA (deg)	Dec. (deg)	Catalogue	G_{av}	Sep. (arcsec)	Comment
HSC J0001+0301	0.489217	3.029465	AW, MQ, HW	2.0	1.730	
HSC J0003−0010	0.923763	−0.169828	HW	2.0	1.025	
HSC J0007+0415	1.816698	4.262469	HW	2.0	1.193	
HSC J0150−0018	27.647481	−0.315818	HW	2.0	1.530	
HSC J0150+0222	27.681565	2.377538	HW	2.0	1.033	
HSC J0833+0105	128.464891	1.098478	HW	2.0	1.444	
HSC J0839+0102	129.949813	1.044056	HW	2.0	1.132	
HSC J0843−0153	130.782963	−1.886293	HW	2.0	1.118	
HSC J0850+0429	132.512991	4.490062	HW	2.0	1.000	
HSC J0902+0441	135.551417	4.684906	HW	2.0	0.994	
HSC J0914+0210	138.676621	2.171698	HW	2.0	2.031	
HSC J0915+0407	138.824936	4.129746	HW	2.0	1.234	
HSC J0919+0418	139.769742	4.300708	HW	2.0	1.383	
HSC J0931+0029	142.993395	0.495155	MQ, HW	2.0	0.852	
HSC J0938−0211	144.521668	−2.198314	HW	2.0	1.377	
HSC J0945+0310	146.359582	3.174973	HW	2.0	1.248	
HSC J0949+0005	147.430346	0.093201	AW, MQ, HW	2.0	1.244	
HSC J1043+0104	160.762983	1.077418	HW	2.0	0.979	
HSC J1104+0121	166.110833	1.350218	HW	2.0	0.975	
HSC J1113−0114	168.419985	−1.238093	HW	2.0	1.351	
HSC J1140+0141	175.065910	1.698669	HW	2.0	0.656	
HSC J1142+0431	175.555705	4.524356	HW	2.0	1.130	
HSC J1151+0229	177.752743	2.483339	HW	2.0	1.532	
HSC J1159+0237	179.866230	2.617025	HW	2.0	1.214	
HSC J1200+0209	180.143132	2.158261	HW	2.0	0.876	
HSC J1201+0436	180.278177	4.605222	HW	2.0	1.402	
HSC J1205+0112	181.498445	1.215812	HW	2.0	0.911	
HSC J1300+0252	195.026033	2.881486	HW	2.0	0.606	
HSC J1307+0011	196.888803	0.189658	HW	2.0	0.833	
HSC J1311+0117	197.828037	1.294614	HW	2.0	1.531	
HSC J1330−0057	202.517777	−0.960672	MQ, HW	2.0	0.763	
HSC J1334−0120	203.546561	−1.347839	MQ, HW	2.0	1.084	[1]: grade B; [2]: grade A
HSC J1341+0009	205.450424	0.152394	MQ, HW	2.0	0.673	
HSC J1349+0322	207.295286	3.375356	HW	2.0	0.965	
HSC J1352−0210	208.040787	−2.169167	MQ, HW	2.0	0.848	
HSC J1353−0007	208.358868	−0.125164	HW	2.0	0.708	
HSC J1355+0045	208.817689	0.764456	MQ, HW	2.0	0.939	
HSC J1401+0207	210.410831	2.127656	HW	2.0	1.297	
HSC J1406−0112	211.593509	−1.208570	AW, MQ, HW	2.0	1.216	Contam.
HSC J1410+0011	212.686693	0.188742	HW	2.0	0.670	
HSC J1417+0221	214.358177	2.363329	AW, HW	2.0	0.740	
HSC J1422+0137	215.677668	1.616869	HW	2.0	0.576	
HSC J1423−0015	215.960533	−0.257750	HW	2.0	1.052	
HSC J1438−0206	219.626823	−2.102920	HW	2.0	0.965	
HSC J1440+0412	220.069873	4.213264	HW	2.0	1.323	
HSC J1524+4211	231.036248	42.198821	HW	2.0	1.258	
HSC J1549+4406	237.485191	44.112865	HW	2.0	0.976	
HSC J1558+4234	239.557764	42.568490	HW	2.0	0.914	
HSC J1619+4445	244.983399	44.762640	HW	2.0	1.436	
HSC J2205+0031	331.254923	0.523038	MQ, HW	2.0	1.074	Contam.
HSC J2219+0110	334.994433	1.178695	AW, MQ, HW	2.0	1.959	
HSC J2226+0109	336.535254	1.156081	HW	2.0	0.784	
HSC J2236+0511	339.226277	5.188411	HW	2.0	0.757	
HSC J2307+0356	346.985715	3.935367	HW	2.0	1.377	
HSC J2323+0050	350.819526	0.836751	HW	2.0	1.147	

Note. [1] He et al. (2023), [2] Dawes et al. (2022), and [3] Storfer et al. (2022).

6.16 J0847−0013 (contam.)

This system was first identified as a lens candidate (Inada et al. 2008), but has been confirmed as a dual quasar system (Silverman et al. 2020), as a result from different Mg II line profiles in each component. Even though it requires a galaxy in light modelling, the galaxy turns out to be a host galaxy with a stellar mass $8.5 \times 10^{10}\,M_{\odot}$.

6.17 J0848+0115 (contam.)

This system was initially identified as a lens candidate Inada et al. (2012) with a quasar at redshift $z = 0.646$. But it turns out to be a quasar+galaxy+star system (commented in GLQD).

6.18 J0947+0247 (contam.)

This system was first identified as a lens candidate in SQLS (Inada et al. 2010), but later confirmed as a quasar ($z = 0.643$) + star (Lemon et al. 2022).

6.19 J1008+0351 (contam.)

This system was first identified as a lens candidate in SQLS (Inada et al. 2008), but later confirmed as a quasar pair with redshifts of $z = 1.745$ and $z = 1.740$ (Kayo & Oguri 2012).

6.20 J1406−0112 (contam.)

This system with a quasar at redshift $z = 1.154$ was initially identified as a lens candidate in SQLS (Inada et al. 2008). However, it was later classified as a contaminant in GLQD due to the absence of a lensing galaxy.

6.21 J2205+0031 (contam.)

This system was classified as a lens candidate (Treu et al. 2018), but later commented as a quasar pair with redshifts of $z = 1.653$ and $z = 1.869$ in GLQD.

7 SUMMARY

In this work, we introduce new candidates for lensed quasars in HSC DR4 S21A, covering an area of approximately 1300 $\deg^2$. We draw the following conclusions:

(i) To identify possible quasar sources, we utilize HSC + unWISE photometry (*grizy* + *W*1 + *W*2) and apply colour cuts that enable us to exclude the vast majority of stars while including most quasars with redshifts $z < 3.5$. In addition, we incorporate two existing quasar catalogues (MILLIQUAS and AllWISEAGN), resulting in a total of 1 652 329 objects.

(ii) Using an efficient classification method developed in Chan et al. (2022), modified to better suit the HSC imaging, we are able to recover 18 of 22 known lenses.

(iii) We visually inspected 121 511 candidates and identified 6199 systems with lensing features, which are graded on a scale of 0 (non-lens) to 3 (lens).

(iv) For the 162 candidates with an average grade of $G_{\rm av} \geq 2$, we conducted light modelling, and 10 systems showing quadruply lensed images were further modelled to determine the image configuration.

(v) Based on the light and lens modelling results, we assigned final grades of A, B, and C, resulting in 57, 15, and 53 candidates, respectively, after the known contaminants are removed.

Despite the lack of spectroscopic information to confirm the nature of our candidates, a viable strategy for follow-up observations is through long-slit spectroscopy using existing instruments. Additionally, these candidates present excellent targets for the Prime Focus Spectrograph, which covers the same area as the HSC and offers the potential to obtain high-quality spectroscopic data. By analysing these data, we can gain a more accurate understanding of the properties of the lensing systems identified in this study. Our successful identification of promising lensed quasar candidates in this work indicates that our classification method can be applied to higher resolution imaging data in the future, such as Euclid and the Vera C. Rubin Observatory's Legacy Survey of Space and Time (LSST), and could lead to the discovery of lenses with the narrowest separation on the sky.

ACKNOWLEDGEMENTS

We thank the anonymous reviewer for careful reading and positive comments. JHHC thanks F. Courbin, C. Lemon, Y.-P. Shu, J. Silverman, Q. Minor, and C. Rusu for useful discussions. This research was made possible by the generosity of Eric and Wendy Schmidt by recommendation of the Schmidt Futures programme. DC was supported by the Tenure Track Pilot Programme of the Croatian Science Foundation and the Ecole Polytechnique Fédérale de Lausanne and the Project TTP-2018-07-1171 'Mining the Variable Sky', with funds of the Croatian-Swiss Research Programme. IC was supported by the National Science and Technology Council in Taiwan (Grant NSTC 111-2112-M-006-037-MY3). ATJ was supported by the Program Riset ITB 2023. SHS thanks the Max Planck Society for support through the Max Planck Research Group and the Max Planck Fellowship. This work was supported by JSPS KAKENHI Grants: Number JP20K14511 for KCW, Number JP20K04016 for IK, and Numbers JP22H01260, JP20H05856, and JP20H00181 for MO.

The Hyper Suprime-Cam collaboration includes the astronomical communities of Japan and Taiwan, and Princeton University. The HSC instrumentation and software were developed by the National Astronomical Observatory of Japan (NAOJ), the Kavli Institute for the Physics and Mathematics of the Universe (Kavli IPMU), the University of Tokyo, the High Energy Accelerator Research Organization (KEK), the Academia Sinica Institute for Astronomy and Astrophysics in Taiwan (ASIAA), and Princeton University. Funding was contributed by the FIRST programme from the Japanese Cabinet Office, the Ministry of Education, Culture, Sports, Science and Technology (MEXT), the Japan Society for the Promotion of Science (JSPS), Japan Science and Technology Agency (JST), the Toray Science Foundation, NAOJ, Kavli IPMU, KEK, ASIAA, and Princeton University.

This paper is based on data collected at the Subaru Telescope and retrieved from the HSC data archive system, which is operated by Subaru Telescope and Astronomy Data Center (ADC) at NAOJ. Data analysis was in part carried out with the cooperation of Center for Computational Astrophysics (CfCA) at NAOJ. We are honoured and grateful for the opportunity of observing the Universe from Maunakea, which has the cultural, historical and natural significance in Hawaii.

This paper makes use of software developed for Vera C. Rubin Observatory. We thank the Rubin Observatory for making their code available as free software at http://pipelines.lsst.io/.

The Pan-STARRS1 Surveys (PS1) and the PS1 public science archive have been made possible through contributions by the Institute for Astronomy, the University of Hawaii, the Pan-STARRS Project Office, the Max Planck Society and its participating insti-

tutes, the Max Planck Institute for Astronomy, Heidelberg, and the Max Planck Institute for Extraterrestrial Physics, Garching, The Johns Hopkins University, Durham University, the University of Edinburgh, the Queen's University Belfast, the Harvard-Smithsonian Center for Astrophysics, the Las Cumbres Observatory Global Telescope Network Incorporated, the National Central University of Taiwan, the Space Telescope Science Institute, the National Aeronautics and Space Administration under grant no. NNX08AR22G issued through the Planetary Science Division of the NASA Science Mission Directorate, the National Science Foundation grant no. AST-1238877, the University of Maryland, Eotvos Lorand University (ELTE), the Los Alamos National Laboratory, and the Gordon and Betty Moore Foundation.

DATA AVAILABILITY

The data underlying this article will be shared on reasonable request to the corresponding author.

REFERENCES

Agnello A. et al., 2018, MNRAS, 479, 4345
Ahumada R. et al., 2020, ApJS, 249, 3
Aihara H. et al., 2018, PASJ, 70, S8
Bosch J. et al., 2018, PASJ, 70, S5
Cantale N., Courbin F., Tewes M., Jablonka P., Meylan G., 2016, A&A, 589, A81
Casey-Clyde J. A., Mingarelli C. M. F., Greene J. E., Pardo K., Nañez M., Goulding A. D., 2021, ApJ, 924, 93
Chan J. H. H., Suyu S. H., Chiueh T., More A., Marshall P. J., Coupon J., Oguri M., Price P., 2015, ApJ, 807, 138
Chan J. H. H. et al., 2020, A&A, 636, A87
Chan J. H. H. et al., 2022, A&A, 659, A140
Chen G. C. F. et al., 2019, MNRAS, 490, 1743
Croom S. M. et al., 2009, MNRAS, 392, 19
Dalal N., Kochanek C. S., 2002, ApJ, 572, 25
Dawes C., Storfer C., Huang X., Aldering G., Dey A., Schlegel D. J., 2022, preprint (arXiv:2208.06356)
Dey A. et al., 2019, AJ, 157, 168
Di Valentino E. et al., 2021, Class. Quant. Grav., 38, 153001
Diehl H. T. et al., 2017, ApJS, 232, 15
Ducourant C. et al., 2018a, in Recio-Blanco A., de Laverny P., Brown A. G. A., Prusti T., eds, Proc. IAU Symp.12 , Astrometry and Astrophysics in the Gaia Sky. p. 59
Ducourant C. et al., 2018b, A&A, 618, A56
Flesch E. W., 2021, VizieR Online Data Catalog, p. VII/290
Freedman W. L., 2021, ApJ, 919, 16
Gaia Collaboration 2016, A&A, 595, A1
Gaia Collaboration 2022, preprint (arXiv:2208.00211)
Gilman D., Birrer S., Treu T., Nierenberg A., Benson A., 2019, MNRAS, 487, 1618
Goulding A. D., Pardo K., Greene J. E., Mingarelli C. M. F., Nyland K., Strauss M. A., 2019, ApJ, 879, L21
He Z., Li N., Cao X., Li R., Zou H., Dye S., 2023, A&A, 672, A123
Ibata R. A. et al., 2017, ApJ, 848, 128
Inada N. et al., 2003, AJ, 126, 666
Inada N. et al., 2008, AJ, 135, 496
Inada N. et al., 2010, AJ, 140, 403
Inada N. et al., 2012, AJ, 143, 119
Jackson N. et al., 1995, MNRAS, 274, L25
Jackson N., Ofek E. O., Oguri M., 2008, MNRAS, 387, 741
Jackson N., Rampadarath H., Ofek E. O., Oguri M., Shin M.-S., 2012, MNRAS, 419, 2014
Jaelani A. T. et al., 2020, MNRAS, 495, 1291
Jaelani A. T. et al., 2021, MNRAS, 502, 1487
Kayo I., Oguri M., 2012, MNRAS, 424, 1363
Khramtsov V. et al., 2019, A&A, 632, A56
Krone-Martins A. et al., 2018, A&A, 616, L11
Lawrence A. et al., 2007, MNRAS, 379, 1599
Lemon C. A., Auger M. W., McMahon R. G., Ostrovski F., 2018, MNRAS, 479, 5060
Lemon C. A., Auger M. W., McMahon R. G., 2019, MNRAS, 483, 4242
Lemon C. et al., 2022, MNRAS, 520, 3305
McMahon R., Irwin M., Hazard C., 1992, GEMINI Newsl. R. Greenwich Obs., 36, 1
Meisner A. M., Lang D., Schlegel D. J., 2018, Res. Notes Am. Astron. Soc., 2, 1
Miyazaki S. et al., 2018, PASJ, 70, S1
Moffat A. F. J., 1969, A&A, 3, 455
More A. et al., 2016, MNRAS, 456, 1595
Morokuma T. et al., 2007, AJ, 133, 214
Myers S. T. et al., 2003, MNRAS, 341, 1
Nierenberg A. M. et al., 2017, MNRAS, 471, 2224
Ochsenbein F., Bauer P., Marcout J., 2000, A&AS, 143, 23
Oguri M., 2010, PASJ, 62, 1017
Oguri M., Marshall P. J., 2010, MNRAS, 405, 2579
Oguri M. et al., 2004, PASJ, 56, 399
Oguri M. et al., 2006, AJ, 132, 999
Oguri M. et al., 2008, AJ, 135, 520
Oguri M. et al., 2012, AJ, 143, 120
Peters C. M. et al., 2015, ApJ, 811, 95
Refsdal S., 1964, MNRAS, 128, 307
Rigby J. R., Bayliss M. B., Gladders M. D., Sharon K., Wuyts E., Dahle H., 2014, ApJ, 790, 44
Rojas K. et al., 2022, A&A, 668, A73
Schlafly E. F., Meisner A. M., Green G. M., 2019, ApJS, 240, 30
Secrest N. J., Dudik R. P., Dorland B. N., Zacharias N., Makarov V., Fey A., Frouard J., Finch C., 2015, ApJS, 221, 12
Sérsic J. L., 1963, Bol. Assoc. Argentina Astron. Plata Argentina, 6, 41
Silverman J. D. et al., 2020, ApJ, 899, 154
Sonnenfeld A. et al., 2018, PASJ, 70, S29
Sonnenfeld A., Jaelani A. T., Chan J. H. H., More A., Suyu S. H., Wong K. C., Oguri M., Lee C.-H., 2019, A&A, 630, A71
Sonnenfeld A. et al., 2020, A&A, 642, A148
Spiniello C. et al., 2018, MNRAS, 480, 1163
Stetson P. B., 1987, PASP, 99, 191
Storfer C. et al., 2022, preprint (arXiv:2206.02764)
Suyu S. H. et al., 2012, ApJ, 750, 10
Treu T. et al., 2018, MNRAS, 481, 1041
Uchiyama H. et al., 2022, ApJ, 934, 68
Vegetti S., Lagattuta D. J., McKean J. P., Auger M. W., Fassnacht C. D., Koopmans L. V. E., 2012, Nature, 481, 341
Verde L., Treu T., Riess A. G., 2019, Nat. Astron., 3, 891
Wenger M. et al., 2000, A&AS, 143, 9
Williams P. R. et al., 2018, MNRAS, 477, L70
Wong K. C. et al., 2018, ApJ, 867, 107
Wong K. C. et al., 2020, MNRAS, 498, 1420
Wong K. C., Chan J. H. H., Chao D. C. Y., Jaelani A. T., Kayo I., Lee C.-H., More A., Oguri M., 2022, PASJ, 74, 1209
Wright E. L. et al., 2010, AJ, 140, 1868
Wu X.-B., Hao G., Jia Z., Zhang Y., Peng N., 2012, AJ, 144, 49

APPENDIX A: GRADE G CANDIDATES

We identify several lensed galaxy candidates, including J0004−0103, which has been previously rediscovered in multiple studies. Although our classification algorithm is primarily designed for lensed quasars, it can also identify these lensed galaxies. The results of lensed galaxy candidates are presented in Fig. A1 and Table A1.

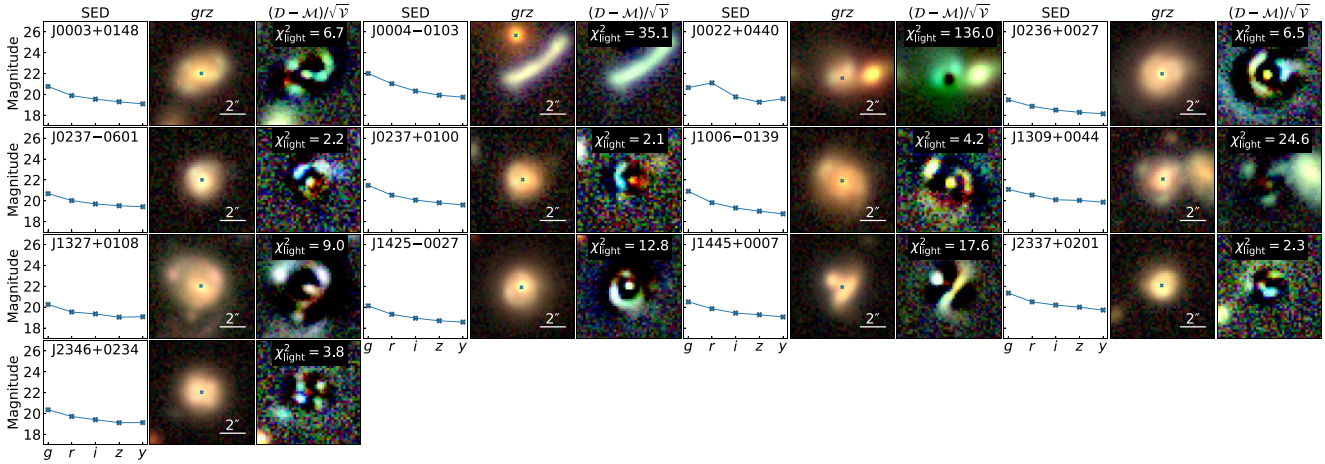

Figure A1. Lensed candidates classified as grade G.

Table A1. Lensed candidates classified as grade G.

Name	RA (deg)	Dec. (deg)	Catalogue	$G_{\rm av}$	Sep. (arcsec)	Comment
HSC J0003+0148	0.906219	1.809688	HW	2.0	–	
HSC J0004−0103	1.215422	−1.055847	HW	3.0	–	[1]; [2]; [3]; [4]
HSC J0022+0440	5.588780	4.676942	HW	2.0	–	
HSC J0236+0027	39.113801	0.452857	HW	2.0	–	
HSC J0237−0601	39.306872	−6.019017	HW	2.0	–	
HSC J0237+0100	39.351162	1.003299	HW	2.0	–	
HSC J1006−0139	151.658371	−1.656651	HW	2.0	–	
HSC J1309+0044	197.255413	0.735544	HW	2.0	–	
HSC J1327+0108	201.815430	1.141450	HW	2.0	–	
HSC J1425−0027	216.317865	−0.459895	HW	2.0	–	
HSC J1445+0007	221.294207	0.119777	HW	2.0	–	
HSC J2337+0201	354.458692	2.020022	HW	2.0	–	
HSC J2346+0234	356.526338	2.571419	HW	2.0	–	

Note. [1] Rigby et al. (2014), [2] Diehl et al. (2017), [3] Jaelani et al. (2020), and [4] Rojas et al. (2022).

APPENDIX B: RESULT FROM LIGHT MODELLING

For lens candidates with $G_{\rm av} \geq 2$ listed in Table B1, we measure the HSC astrometry and photometry via light modelling (see Section 5).

Table B1. Result of light modelling for the candidates with $G_{\rm av} \geq 2$.

Name	Comp.	$\Delta\alpha$ (arcsec)	$\Delta\delta$ (arcsec)	HSC-*g*	HSC-*r*	HSC-*i*	HSC-*z*	HSC-*y*
HSC J0015+0145 [A]	*A*	−0.056	−0.365	20.45	20.07	20.03	20.00	19.82
	B	0.115	0.631	21.56	21.04	20.98	20.71	20.44
	G	−0.191	0.331	20.74	19.76	19.33	19.10	18.78
HSC J0025−0027 [A]	*A*	0.286	−1.231	23.98	23.06	22.47	21.98	21.49
	B	0.627	0.947	25.65	23.52	22.34	21.86	21.46
	G	−0.053	−0.095	20.79	20.29	19.95	19.76	19.67
HSC J0047+0322 [A]	*A*	0.079	−0.275	21.86	21.79	21.61	21.38	21.41
	B	−0.785	1.003	22.06	22.01	21.89	21.63	21.68
	G	−0.143	0.107	22.54	21.02	20.15	19.72	19.48
HSC J0101−0130 [A]	*A*	−0.110	−0.011	20.34	20.02	20.01	19.96	20.00
	B	−1.031	−1.703	22.93	22.45	22.52	22.47	22.97
	G	−0.357	−1.206	21.12	19.97	19.32	18.99	18.83
HSC J0117+0056 [A]	*A*	−1.624	−0.538	22.03	21.58	21.44	21.35	21.30
	B	0.313	−0.089	22.41	22.23	21.88	21.87	21.92
	G	−0.211	−0.032	21.25	20.69	20.14	19.86	19.73
HSC J0122+0037 [A]	*A*	−0.454	−0.908	23.41	23.06	23.18	22.60	22.93
	B	−0.015	−0.847	24.26	23.37	23.26	23.26	23.08
	C	−0.715	0.623	24.16	23.99	23.90	22.92	23.74
	D	0.673	0.122	25.05	24.60	24.68	25.27	24.82
	G	−0.156	−0.048	21.13	20.18	19.80	19.45	19.40
HSC J0126+0136 [A]	*A*	−1.165	0.195	22.89	22.96	22.65	22.88	22.87
	B	−0.451	0.808	23.02	23.08	22.64	22.76	22.82
	C	0.212	0.807	22.59	22.76	22.35	22.65	22.64
	D	−0.211	−1.085	22.50	22.67	22.43	22.45	22.43
	G	0.002	−0.117	19.22	18.84	18.58	18.45	18.38
HSC J0130+0010 [A]	*A*	−0.621	−0.125	22.35	22.46	22.08	21.88	22.37
	B	0.285	0.347	22.60	22.41	21.85	21.58	21.89
	G	0.040	−0.213	21.23	20.68	20.16	19.90	19.70
HSC J0130+0120 [A]	*A*	−0.065	0.355	22.85	22.53	22.62	22.47	21.66
	B	−0.036	−0.813	23.34	22.64	22.38	22.27	21.73
	G	0.014	−0.004	22.15	21.13	20.69	20.45	20.13
HSC J0138+0315 [A]	*A*	−0.126	−0.146	21.81	21.12	21.14	20.50	20.61
	B	−1.861	0.913	21.95	21.21	20.98	20.74	20.43
	G	−0.508	0.428	22.44	21.76	21.27	20.78	20.74
HSC J0141+0039 [A]	*A*	−0.540	−0.106	22.63	22.77	22.63	22.34	22.47
	B	0.455	0.046	22.75	22.72	22.39	21.95	22.08
	G	−0.206	−0.064	23.60	21.84	20.67	20.23	20.08
HSC J0202+0143 [A]	*A*	−0.718	1.235	20.02	20.22	20.14	20.15	19.99
	B	−0.887	−1.485	20.38	21.34	21.00	21.69	21.30
	G	−0.297	0.182	18.86	18.94	18.71	18.84	18.68
HSC J0222−0156 [A]	*A*	−0.820	−0.926	23.76	23.45	23.41	23.21	23.21
	B	−0.861	0.821	24.26	23.60	23.34	22.97	23.01
	C	−1.287	0.286	24.41	24.03	23.85	23.21	23.27
	D	0.210	−0.024	23.34	22.36	21.94	21.66	21.55
	G	−0.335	−0.025	21.55	20.55	20.20	19.92	19.85
HSC J0224+0247 [A]	*A*	−0.201	−0.165	21.80	20.91	21.07	20.77	20.94
	B	0.449	0.515	22.50	21.62	21.43	21.23	21.31
	G	1.117	−0.679	22.66	20.57	19.91	19.48	19.18
HSC J0847−0013 [A]	*A*	−0.105	−0.019	19.97	19.68	19.36	19.34	19.31
	B	−0.689	−0.840	20.30	20.16	19.66	19.66	19.49
	G	−0.307	−0.190	20.78	19.84	19.19	19.04	18.79
HSC J0848+0115 [A]	*A*	−0.070	−0.083	19.18	19.32	19.34	19.34	19.32
	B	−0.258	−1.492	20.37	19.98	19.83	19.75	19.73
	G	0.713	−0.871	21.19	20.42	19.65	19.30	19.07
HSC J0904−0053 [A]	*A*	−1.359	−1.868	21.14	20.82	20.65	20.63	20.56
	B	−0.137	−0.047	21.74	21.24	21.11	21.03	20.99
	G	−0.266	−0.864	23.71	23.27	22.15	21.54	20.73
HSC J0911−0044 [A]	*A*	−0.035	−0.125	21.89	21.48	21.06	20.63	20.28
	B	−0.227	−1.289	21.64	21.33	20.90	20.52	20.15
	G	0.025	−0.878	22.68	22.17	21.34	20.78	20.65
HSC J0939−0214 [A]	*A*	−0.121	−0.032	20.80	20.58	20.52	20.48	20.45
	B	−1.828	−1.222	21.46	21.22	21.06	21.03	20.68
	G	−1.591	−1.080	23.00	21.17	20.35	19.99	19.73
HSC J0954−0022 [A]	*A*	−0.107	−0.045	20.97	20.91	20.64	20.13	20.14

Table B1 – *continued*

Name	Comp.	$\Delta\alpha$ (arcsec)	$\Delta\delta$ (arcsec)	HSC-*g*	HSC-*r*	HSC-*i*	HSC-*z*	HSC-*y*
	B	0.026	− 1.299	22.13	22.08	22.09	21.52	21.65
	G	0.083	− 0.666	24.01	25.09	22.07	22.29	21.84
HSC J0956+0503 [A]	*A*	− 1.980	− 1.100	21.29	20.71	20.38	20.26	20.14
	B	− 0.078	− 0.017	20.11	19.87	19.57	19.55	19.52
	G	− 0.254	− 0.018	21.17	20.30	19.79	19.45	19.33
HSC J0956−0020 [A]	*A*	− 2.182	− 0.237	22.41	22.07	22.20	22.53	22.70
	B	0.660	0.014	22.30	22.25	22.40	22.50	22.37
	G	− 0.147	− 0.184	19.79	19.38	19.25	19.21	19.08
HSC J1026−0139 [A]	*A*	− 1.192	0.065	23.60	22.91	22.28	22.13	21.75
	B	− 0.112	− 0.084	22.68	22.98	22.33	21.97	21.48
	G	− 0.379	0.157	23.01	22.40	21.41	20.95	20.79
HSC J1114+0011 [A]	*A*	− 0.051	− 0.146	20.64	20.23	20.14	20.07	20.09
	B	0.193	− 3.149	20.36	20.08	19.94	19.93	19.91
	G	− 0.211	− 1.048	22.81	22.79	22.26	22.04	21.48
HSC J1115+0321 [A]	*A*	− 0.376	− 0.583	22.64	22.24	21.96	21.83	21.78
	B	− 0.012	0.255	23.20	22.64	22.03	21.95	21.50
	G	− 0.067	− 0.039	22.73	22.16	21.48	20.77	20.67
HSC J1127+0424 [A]	*A*	0.023	− 0.239	22.18	22.06	22.04	21.94	21.55
	B	− 0.323	− 0.057	22.51	22.48	22.40	22.36	21.93
	C	− 0.749	− 1.264	22.79	22.71	22.67	22.73	22.33
	D	− 1.490	− 0.449	23.05	23.13	23.12	23.02	22.79
	G	− 0.624	− 0.907	22.23	21.69	20.88	20.23	19.88
HSC J1153+0007 [A]	*A*	− 0.529	− 0.021	20.95	20.35	20.07	19.96	19.87
	B	0.072	− 0.098	21.34	20.86	20.50	20.68	20.61
	G	0.041	− 0.255	20.10	19.31	18.87	18.61	18.45
HSC J1215+0047 [A]	*A*	− 0.056	− 0.034	21.77	21.81	21.83	21.40	21.53
	B	− 2.662	0.833	22.97	23.05	22.87	22.29	22.13
	G	− 1.887	0.796	22.57	20.84	19.59	19.19	18.96
HSC J1220+0112 [A]	*A*	− 0.399	1.274	21.66	21.60	21.43	21.38	21.28
	B	0.090	− 0.580	22.50	22.37	22.07	22.12	21.88
	G	− 0.197	− 0.018	22.14	20.77	19.86	19.48	19.22
HSC J1232+0159 [A]	*A*	− 0.237	0.573	22.18	22.02	21.99	21.57	21.51
	B	0.099	− 0.153	22.25	22.06	22.08	21.61	21.45
	C	0.219	− 0.962	22.30	22.14	22.08	21.60	21.56
	G	− 0.792	− 0.324	24.18	23.31	20.72	20.64	20.27
HSC J1241+0002 [A]	*A*	− 0.033	− 0.119	21.56	21.36	21.36	21.32	21.22
	B	− 1.371	− 2.196	23.56	23.15	23.11	23.28	23.22
	G	− 1.154	− 1.864	22.60	21.97	21.42	21.39	21.26
HSC J1242+0239 [A]	*A*	1.208	2.469	21.78	21.28	20.87	20.48	20.35
	B	− 0.074	− 0.178	21.24	20.85	20.55	20.25	20.18
	G	0.198	0.872	22.63	20.66	20.72	20.58	19.92
HSC J1252+0357 [A]	*A*	0.785	− 0.983	23.08	22.66	22.41	22.33	22.15
	B	− 1.152	0.795	23.74	23.45	22.96	22.94	22.84
	G	− 0.154	− 0.017	19.82	19.03	18.60	18.41	18.26
HSC J1258+0416 [A]	*A*	− 0.759	− 0.906	22.18	21.58	21.36	21.22	21.12
	B	− 0.045	− 0.099	20.62	20.65	20.80	20.54	20.58
	G	0.125	0.128	21.86	21.29	20.49	20.15	20.12
HSC J1314+0157 [A]	*A*	− 0.067	− 0.144	21.99	21.60	20.98	21.94	21.82
	B	− 1.310	0.569	22.44	22.15	21.75	22.16	22.10
	G	− 0.391	0.262	22.34	21.85	21.65	21.74	21.53
HSC J1320+0320 [A]	*A*	− 0.013	− 0.370	21.94	21.63	21.38	21.32	21.21
	B	− 0.074	0.883	22.66	22.30	22.45	22.55	22.38
	G	− 0.108	0.224	22.15	21.07	20.70	20.42	20.25
HSC J1350+4218 [A]	*A*	− 0.099	− 0.109	20.32	20.40	20.21	20.18	20.05
	B	− 0.557	− 0.675	21.33	21.11	21.33	21.18	21.27
	G	− 0.437	− 0.330	23.37	21.46	20.59	20.37	20.04
HSC J1408−0133 [A]	*A*	2.619	0.028	24.37	22.97	21.88	21.33	21.04
	B	− 0.864	− 0.600	25.52	24.88	23.97	24.09	23.46
	G	− 0.029	− 0.091	20.00	19.65	19.36	19.25	19.11
HSC J1418+0018 [A]	*A*	0.017	− 0.203	24.03	23.39	23.00	22.76	22.78
	B	− 0.168	1.920	22.93	22.44	21.92	22.11	21.54
	G	− 0.089	0.077	22.56	21.73	21.27	21.08	20.89
HSC J1421+4253 [A]	*A*	− 0.008	− 0.504	23.50	23.03	22.93	22.81	22.50

Table B1 – *continued*

Name	Comp.	$\Delta\alpha$ (arcsec)	$\Delta\delta$ (arcsec)	HSC-*g*	HSC-*r*	HSC-*i*	HSC-*z*	HSC-*y*
	B	− 0.000	1.013	23.84	23.06	22.85	22.74	22.65
	G	− 0.067	0.001	21.09	20.21	19.87	19.56	19.36
HSC J1428−0118 [A]	*A*	1.894	0.955	19.70	19.44	19.24	19.32	19.27
	B	− 0.389	− 0.559	22.62	22.19	22.00	21.86	21.82
	G	− 0.053	− 0.021	20.68	20.16	19.93	19.76	19.66
HSC J1432+4337 [A]	*A*	0.196	− 0.019	23.15	22.44	22.33	22.21	22.31
	B	− 0.152	− 0.257	23.04	22.79	22.76	22.63	22.09
	C	− 0.872	− 0.015	23.05	22.60	22.61	22.44	22.38
	D	− 0.372	1.107	22.68	22.26	22.28	22.16	21.99
	G	− 0.386	0.436	21.97	21.50	21.20	20.90	20.44
HSC J1436−0026 [A]	*A*	− 0.323	− 0.023	22.04	21.69	21.55	21.64	21.61
	B	0.567	0.335	22.79	22.34	22.15	22.51	22.42
	G	0.003	− 0.070	21.01	20.67	20.42	20.53	20.26
HSC J1446−0146 [A]	*A*	1.980	1.525	20.14	20.06	20.11	20.13	20.12
	B	− 0.158	− 0.133	21.32	20.81	20.69	20.58	20.52
	G	0.373	− 0.172	20.35	19.48	19.03	18.80	18.63
HSC J1450+0358 [A]	*A*	− 0.401	0.196	22.24	21.87	21.68	21.60	21.45
	B	0.247	− 0.573	22.61	22.18	21.81	21.72	21.55
	G	0.052	− 0.085	22.26	21.63	20.93	20.52	20.11
HSC J1453+0039 [A]	*A*	− 0.027	− 0.042	20.24	20.06	20.07	20.20	20.14
	B	0.741	0.473	22.02	21.60	21.54	21.55	21.39
	G	− 0.242	− 0.002	23.97	22.27	21.52	20.55	20.16
HSC J1527+4308 [A]	*A*	− 0.066	0.005	21.43	20.89	20.75	20.65	20.61
	B	− 1.380	− 0.066	21.99	21.59	21.71	21.74	21.79
	G	− 1.030	− 0.127	23.63	23.68	22.11	21.60	21.34
HSC J1633+4235 [A]	*A*	− 0.163	− 0.046	20.43	19.98	19.83	19.62	19.54
	B	1.979	− 1.496	20.42	20.13	20.00	20.02	19.86
	G	1.132	− 1.069	23.57	22.56	22.09	21.77	21.25
HSC J2204+0434 [A]	*A*	− 0.019	− 0.051	21.21	20.80	20.42	20.26	20.20
	B	− 0.581	− 2.242	22.99	22.27	21.70	21.47	21.35
	G	− 0.519	− 1.579	25.17	22.53	21.19	20.37	20.03
HSC J2204−0118 [A]	*A*	− 0.421	− 1.033	22.90	22.76	22.49	22.35	22.10
	B	− 0.051	0.481	22.62	22.42	22.32	22.14	21.91
	G	0.004	− 0.184	22.04	20.70	19.88	19.48	19.23
HSC J2212−0103 [A]	*A*	1.573	1.350	20.57	20.25	20.15	20.08	20.05
	B	− 0.008	− 0.140	21.02	20.82	20.70	20.35	20.47
	G	0.854	0.257	23.89	23.34	22.72	22.61	22.31
HSC J2220+0050 [A]	*A*	− 0.786	− 0.275	23.01	22.71	22.64	22.70	22.63
	B	− 0.152	− 0.731	23.53	23.02	22.89	22.88	22.97
	C	0.028	1.204	24.66	23.81	23.54	23.41	23.39
	D	1.476	− 0.593	23.99	22.99	22.52	22.21	22.08
	G	0.035	0.114	21.16	20.27	19.69	19.40	19.12
HSC J2225+0409 [A]	*A*	− 0.035	− 0.162	21.42	21.42	21.39	21.37	21.51
	B	− 0.210	1.456	21.47	21.01	20.81	20.67	20.60
	G	− 0.163	− 0.032	22.48	21.71	20.68	20.25	19.94
HSC J2246+0027 [A]	*A*	− 0.968	− 1.883	27.38	25.88	23.60	22.58	22.08
	B	− 1.022	0.469	25.16	23.97	22.13	21.31	20.96
	G	− 0.043	− 0.071	21.36	20.61	20.20	19.96	19.82
HSC J2256+0125 [A]	*A*	− 0.600	− 0.333	22.97	22.80	22.92	22.44	23.16
	B	− 0.397	0.261	23.03	22.94	22.92	22.66	22.58
	C	0.099	0.362	23.23	22.95	22.73	22.21	22.45
	D	0.369	− 0.301	23.68	23.33	22.82	22.33	22.33
	G	− 0.129	− 0.180	21.88	21.22	20.42	19.97	19.76
HSC J2321+0314 [A]	*A*	− 0.417	− 1.364	22.87	22.60	22.10	22.77	22.62
	B	0.020	− 0.108	22.96	22.42	22.00	21.83	21.73
	G	− 0.821	− 0.740	22.48	21.75	21.27	21.37	21.35
HSC J2330+0458 [A]	*A*	− 0.165	0.346	21.99	21.52	21.26	21.20	21.17
	B	0.058	− 0.560	22.16	21.81	21.52	21.56	21.35
	G	0.042	− 0.064	21.40	21.07	20.57	20.13	20.15
HSC J2335−0050 [A]	*A*	0.710	− 0.529	22.74	21.88	21.56	21.30	20.91
	B	1.004	− 0.091	24.31	22.98	22.57	22.15	21.84
	C	0.199	0.984	24.09	22.87	22.20	21.77	21.38
	D	− 0.359	− 0.050	27.71	24.41	22.75	21.92	20.61
	G	− 0.104	− 0.060	20.58	19.98	19.35	19.40	18.85

Table B1 – *continued*

Name	Comp.	$\Delta\alpha$ (arcsec)	$\Delta\delta$ (arcsec)	HSC-*g*	HSC-*r*	HSC-*i*	HSC-*z*	HSC-*y*
HSC J2339+0000 [A]	*A*	− 0.021	− 0.244	22.14	22.09	22.12	22.00	21.85
	B	0.263	0.078	22.84	22.82	22.83	22.92	22.66
	C	− 0.345	1.349	23.03	23.12	22.93	22.76	22.55
	D	− 1.044	0.231	23.56	23.49	23.30	23.09	22.75
	G	− 0.369	0.427	21.03	20.72	20.16	19.83	19.56
HSC J0839+0515 [B]	*A*	− 0.038	− 0.087	20.05	19.83	19.73	19.78	19.93
	B	− 0.241	1.737	21.60	21.06	20.76	20.59	20.59
HSC J0913+0518 [B]	*A*	− 0.135	0.018	21.59	21.08	21.05	20.87	20.59
	B	− 0.532	1.577	21.97	21.45	21.45	21.08	21.05
HSC J0915−0041 [B]	*A*	− 0.078	− 0.083	21.35	20.61	20.36	20.23	20.04
	B	− 0.616	− 1.449	23.13	22.17	21.90	21.69	21.41
HSC J0947+0247 [B]	*A*	− 0.867	1.180	19.61	19.49	19.41	19.46	19.39
	B	− 0.019	− 0.040	20.95	20.43	20.23	20.14	20.05
HSC J1003−0219 [B]	*A*	− 0.153	− 0.129	20.99	20.66	20.51	20.53	20.37
	B	− 0.728	1.137	22.05	21.64	21.43	21.33	21.30
HSC J1003−0149 [B]	*A*	0.000	− 0.075	21.00	20.53	20.49	20.36	20.14
	B	− 0.137	− 1.227	21.54	20.83	20.53	20.35	20.23
HSC J1008+0351 [B]	*A*	− 0.167	− 0.064	20.11	19.73	19.20	19.05	19.01
	B	0.207	0.880	21.07	20.95	20.77	20.59	20.54
HSC J1041−0056 [B]	*A*	− 0.098	− 0.030	18.52	18.50	18.43	18.45	17.72
	B	1.498	− 1.229	20.04	19.76	19.67	19.66	19.53
HSC J1202−0214 [B]	*A*	0.174	− 0.067	21.84	21.53	21.42	21.39	21.38
	B	− 0.439	− 0.253	22.43	21.89	21.80	21.88	21.89
HSC J1216+0041 [B]	*A*	− 0.832	− 0.653	22.54	21.83	21.92	21.74	21.66
	B	− 0.122	− 0.066	22.35	21.77	21.81	21.66	21.68
HSC J1338+0406 [B]	*A*	− 0.137	− 0.019	21.10	20.54	20.32	20.18	20.11
	B	− 2.506	− 1.694	22.46	21.60	21.19	21.15	21.03
	C	− 1.672	− 1.124	21.51	20.33	19.05	18.52	18.30
HSC J1426−0203 [B]	*A*	− 0.103	− 0.010	20.53	20.39	19.96	20.01	19.86
	B	− 0.681	− 1.052	22.04	21.62	21.44	21.35	21.28
HSC J1443−0044 [B]	*A*	− 0.979	1.041	20.60	20.25	20.14	20.06	20.02
	G	0.000	− 0.031	21.71	21.28	20.94	20.88	20.77
HSC J1458+4202 [B]	*A*	− 0.026	− 0.106	22.38	21.71	21.48	21.06	21.29
	B	1.036	− 0.731	22.57	21.90	21.65	21.41	21.46
HSC J1505+4426 [B]	*A*	− 0.803	− 0.855	22.15	21.42	21.35	21.18	20.81
	B	− 0.152	− 0.008	22.07	21.49	21.47	21.30	20.80
HSC J1544+4211 [B]	*A*	− 0.558	0.543	20.95	20.69	20.52	20.60	20.20
	B	− 0.055	− 0.122	21.19	21.03	20.91	21.07	20.59
HSC J1547+4211 [B]	*A*	2.017	− 0.514	20.09	19.89	19.71	19.64	19.66
	B	− 0.149	− 0.067	21.81	21.56	21.36	21.25	21.25
HSC J0001+0301 [C]	*A*	− 0.462	1.553	20.42	19.71	19.49	19.19	18.61
	B	− 0.009	− 0.117	21.02	20.60	20.54	20.32	20.38
HSC J0003−0010 [C]	*A*	− 0.589	0.731	21.25	20.43	20.10	19.89	19.78
	B	− 0.070	− 0.154	21.76	20.78	20.37	19.92	19.86
HSC J0007+0415 [C]	*A*	− 0.073	− 0.013	21.29	21.10	20.63	20.50	20.46
	B	− 0.689	− 1.034	21.72	21.44	21.13	21.09	20.98
HSC J0150−0018 [C]	*A*	− 0.104	− 0.065	22.24	21.70	21.53	21.33	21.11
	B	− 0.257	1.457	22.19	21.70	21.73	21.51	21.37
HSC J0150+0222 [C]	*A*	− 0.052	− 0.048	21.25	21.09	20.87	20.47	20.54
	B	0.783	− 0.656	22.20	22.20	21.99	21.76	21.78
HSC J0833+0105 [C]	*A*	− 1.473	− 0.156	18.27	17.92	17.86	17.81	17.78
	B	− 0.031	− 0.094	20.05	19.56	19.39	19.30	19.23
HSC J0839+0102 [C]	*A*	− 1.096	0.425	18.73	18.39	18.32	18.27	18.25
	B	− 0.116	− 0.142	20.16	19.62	19.45	19.30	19.27
HSC J0843−0153 [C]	*A*	− 0.845	− 0.838	20.90	20.72	20.53	20.45	20.26
	B	− 0.047	− 0.055	21.33	20.69	20.57	20.47	20.40
HSC J0850+0429 [C]	*A*	− 0.068	− 0.096	20.20	20.36	20.14	20.02	20.11
	B	0.857	− 0.476	21.53	21.36	21.01	20.89	20.80
HSC J0902+0441 [C]	*A*	− 0.320	− 0.334	22.05	21.53	21.42	21.36	21.19
	B	0.474	0.264	22.72	22.01	21.86	21.80	21.62
HSC J0914+0210 [C]	*A*	− 1.252	1.627	22.66	22.16	21.93	21.62	21.59
	B	− 0.076	− 0.029	22.66	21.94	21.59	21.18	20.98
HSC J0915+0407 [C]	*A*	− 0.282	− 1.347	20.32	19.82	19.68	19.55	19.48
	B	− 0.096	− 0.127	21.41	20.89	20.74	20.61	20.55

Table B1 – *continued*

Name	Comp.	$\Delta\alpha$ (arcsec)	$\Delta\delta$ (arcsec)	HSC-*g*	HSC-*r*	HSC-*i*	HSC-*z*	HSC-*y*
HSC J0919+0418 [C]	*A*	−0.032	−0.002	21.43	21.22	20.80	20.79	20.58
	B	−1.151	−0.815	22.12	21.74	21.64	21.57	21.46
HSC J0931+0029 [C]	*A*	−0.018	−0.147	21.33	21.02	20.77	20.53	20.65
	B	−0.839	0.082	23.19	22.44	21.93	21.37	21.37
HSC J0938−0211 [C]	*A*	−1.195	−0.860	18.88	18.50	18.44	18.37	18.31
	B	−0.030	−0.127	20.32	20.00	19.97	19.87	19.90
HSC J0945+0310 [C]	*A*	−0.066	−0.053	20.17	19.78	19.58	19.43	19.50
	B	−0.865	−1.013	21.48	21.71	21.33	20.89	21.15
HSC J0949+0005 [C]	*A*	−0.994	0.742	18.81	18.58	18.70	18.49	18.32
	B	−0.035	−0.051	20.52	20.09	20.05	19.93	19.83
HSC J1043+0104 [C]	*A*	−0.183	−0.096	20.70	20.43	20.33	20.31	20.22
	B	0.716	−0.482	21.95	21.59	21.36	21.25	20.94
HSC J1104+0121 [C]	*A*	−0.171	−0.066	20.12	19.99	19.87	19.77	19.92
	B	0.116	0.866	21.54	21.10	20.92	20.86	20.77
HSC J1113−0114 [C]	*A*	−0.300	−1.433	20.64	20.27	20.41	20.37	20.17
	B	−0.040	−0.107	22.58	21.96	21.88	21.67	21.69
HSC J1140+0141 [C]	*A*	−0.021	−0.014	20.67	20.58	20.31	20.37	20.40
	B	−0.482	−0.480	21.64	21.38	21.27	21.26	21.25
HSC J1142+0431 [C]	*A*	−0.803	0.634	20.32	20.09	20.01	19.87	19.74
	B	−0.007	−0.167	21.19	20.46	20.17	20.04	19.92
HSC J1151+0229 [C]	*A*	−0.135	−0.094	20.45	20.19	20.07	19.98	20.00
	B	−1.089	1.105	21.03	20.50	20.37	20.24	20.08
HSC J1159+0237 [C]	*A*	0.958	0.342	20.84	20.49	20.43	20.32	20.40
	B	−0.150	−0.156	21.69	21.40	21.47	21.41	21.28
HSC J1200+0209 [C]	*A*	−0.108	−0.083	20.79	20.35	20.23	20.15	20.11
	B	0.462	−0.748	21.37	21.28	20.93	20.93	21.02
HSC J1201+0436 [C]	*A*	0.914	−1.126	19.33	19.09	19.05	19.04	19.03
	B	−0.084	−0.141	21.12	21.04	20.73	20.77	20.74
HSC J1205+0112 [C]	*A*	−0.040	−0.119	21.54	21.17	20.61	20.49	20.51
	B	0.870	−0.083	23.09	22.39	21.68	21.22	21.20
HSC J1300+0252 [C]	*A*	−0.164	−0.152	21.33	21.02	20.92	20.88	20.85
	B	−0.088	0.449	22.22	21.85	21.62	21.60	21.48
HSC J1307+0011 [C]	*A*	−0.078	−0.060	20.18	19.96	20.24	19.90	19.85
	B	−0.907	−0.141	20.94	20.82	20.89	20.67	20.54
HSC J1311+0117 [C]	*A*	−0.153	−0.165	21.98	21.56	21.47	21.32	21.51
	B	−1.234	−1.249	22.39	21.97	21.95	21.83	22.02
HSC J1330−0057 [C]	*A*	−0.080	0.039	21.37	20.97	20.88	20.80	20.76
	B	−0.550	−0.563	21.63	21.52	21.29	21.37	21.34
HSC J1334−0120 [C]	*A*	0.252	−1.039	20.53	20.52	20.57	20.20	20.24
	B	−0.140	−0.029	20.69	20.23	20.24	20.25	20.33
HSC J1341+0009 [C]	*A*	−0.197	0.095	21.56	21.56	21.37	21.33	21.18
	B	0.130	−0.493	21.99	21.89	21.68	21.60	21.41
HSC J1349+0322 [C]	*A*	−0.135	−0.103	19.29	19.08	19.01	19.00	18.97
	B	−1.087	−0.260	20.76	20.73	20.70	20.63	20.65
HSC J1352−0210 [C]	*A*	−0.192	0.168	21.04	20.72	20.81	20.73	20.50
	B	0.017	−0.655	21.75	21.50	21.40	21.34	21.29
HSC J1353−0007 [C]	*A*	−0.351	−0.088	21.46	21.10	21.03	20.97	20.88
	B	0.356	−0.127	22.37	22.04	21.74	21.47	21.29
HSC J1355+0045 [C]	*A*	−0.602	−0.967	21.43	21.05	20.90	20.84	20.79
	B	−0.145	−0.146	21.76	21.20	21.13	20.95	20.94
HSC J1401+0207 [C]	*A*	−0.146	−0.121	21.59	20.67	20.31	20.13	20.07
	B	−0.974	−1.120	21.78	21.50	20.85	20.87	20.63
HSC J1406−0112 [C]	*A*	−0.103	−0.051	19.81	19.18	18.92	18.83	18.56
	B	−1.298	−0.283	20.95	20.62	20.50	20.45	20.31
HSC J1410+0011 [C]	*A*	0.083	−0.381	22.44	22.00	21.59	21.47	21.43
	B	−0.354	0.127	22.65	22.12	21.65	21.50	21.43
HSC J1417+0221 [C]	*A*	−0.058	−0.000	21.37	20.38	20.74	21.68	21.53
	B	−0.564	−0.540	21.88	21.43	21.59	22.19	22.18
HSC J1422+0137 [C]	*A*	0.184	−0.060	20.52	19.73	19.44	19.30	19.21
	B	−0.373	−0.207	21.33	20.35	19.91	19.74	19.59
HSC J1423−0015 [C]	*A*	−0.676	−1.000	21.08	20.66	20.50	20.44	20.37
	B	−0.053	−0.152	22.32	22.28	21.62	21.99	21.73
HSC J1438−0206 [C]	*A*	0.880	−0.213	21.18	20.76	20.59	20.55	20.50
	B	−0.069	−0.035	21.85	21.20	21.02	20.91	20.85

Table B1 – *continued*

Name	Comp.	$\Delta\alpha$ (arcsec)	$\Delta\delta$ (arcsec)	HSC-*g*	HSC-*r*	HSC-*i*	HSC-*z*	HSC-*y*
HSC J1440+0412 [C]	*A*	− 0.022	− 0.163	21.84	20.82	20.63	20.36	20.03
	B	− 0.796	0.910	22.16	21.15	20.93	20.65	20.37
HSC J1524+4211 [C]	*A*	− 0.322	1.214	21.18	20.99	20.82	20.74	20.66
	B	− 0.163	− 0.034	21.90	20.95	20.53	20.34	20.16
HSC J1549+4406 [C]	*A*	− 0.101	− 0.166	20.83	20.58	20.50	20.44	20.45
	B	0.644	0.465	22.19	22.10	21.72	21.51	21.56
HSC J1558+4234 [C]	*A*	− 0.081	− 0.067	20.90	20.48	20.28	20.19	20.18
	B	− 0.768	0.535	20.82	20.78	20.75	20.58	20.51
HSC J1619+4445 [C]	*A*	− 0.053	− 0.111	21.57	20.91	20.60	20.44	20.34
	B	− 1.490	− 0.083	22.76	21.97	21.61	21.38	21.29
HSC J2205+0031 [C]	*A*	− 0.021	− 0.094	20.53	20.31	20.17	20.15	20.19
	B	− 1.095	− 0.095	21.22	20.95	20.89	20.84	20.81
HSC J2219+0110 [C]	*A*	− 0.465	1.924	21.51	20.89	20.32	19.72	19.90
	B	− 0.133	− 0.007	21.15	21.44	20.63	20.23	20.39
HSC J2226+0109 [C]	*A*	− 0.057	− 0.267	20.79	20.46	20.62	20.09	20.38
	B	0.126	0.495	21.05	20.94	20.98	20.50	20.66
HSC J2236+0511 [C]	*A*	0.162	− 0.238	21.65	21.18	20.95	20.88	20.84
	B	− 0.518	0.095	21.96	21.44	21.19	21.10	21.09
HSC J2307+0356 [C]	*A*	− 1.165	− 0.866	20.25	19.91	19.96	19.81	19.61
	B	− 0.031	− 0.085	21.07	20.78	20.63	20.47	20.42
HSC J2323+0050 [C]	*A*	− 0.148	− 0.102	20.87	20.48	20.45	20.51	20.50
	B	− 0.886	0.777	22.48	21.99	21.88	21.58	21.55
HSC J0003+0148 [G]	*G*	− 0.137	− 0.075	20.76	19.89	19.54	19.29	19.09
HSC J0004−0103 [G]	*G*	− 0.549	2.683	22.01	21.02	20.32	19.92	19.73
HSC J0022+0440 [G]	*G*	− 0.086	− 0.417	20.65	21.10	19.76	19.26	19.58
HSC J0236+0027 [G]	*G*	− 0.112	− 0.095	19.48	18.86	18.50	18.28	18.14
HSC J0237−0601 [G]	*G*	− 0.094	− 0.078	20.69	20.02	19.69	19.52	19.43
HSC J0237+0100 [G]	*G*	− 0.048	− 0.060	21.48	20.54	20.06	19.81	19.60
HSC J1006−0139 [G]	*G*	− 0.094	− 0.146	20.91	19.82	19.31	19.00	18.75
HSC J1309+0044 [G]	*G*	− 0.053	− 0.022	21.09	20.55	20.10	20.04	19.87
HSC J1327+0108 [G]	*G*	− 0.162	− 0.055	20.26	19.54	19.35	19.04	19.08
HSC J1425−0027 [G]	*G*	− 0.145	− 0.162	20.12	19.32	18.94	18.69	18.57
HSC J1445+0007 [G]	*G*	− 0.097	− 0.141	20.50	19.85	19.43	19.27	19.06
HSC J2337+0201 [G]	*G*	− 0.141	− 0.022	21.35	20.51	20.20	20.00	19.72
HSC J2346+0234 [G]	*G*	− 0.119	− 0.053	20.36	19.72	19.41	19.12	19.13

This paper has been typeset from a TEX/LATEX file prepared by the author.